Stochastic density functional theory combined with Langevin dynamics for warm dense matter

Rebecca Efrat Hadad
Fritz Haber Research Center for Molecular Dynamics, Institute of Chemistry, The Hebrew University of Jerusalem, Jerusalem 91904, Israel

Argha Roy
Institute of Physics, University of Rostock, 18051 Rostock, Germany

Eran Rabani
Department of Chemistry, University of California, Berkeley, California 94720, USA; Materials Sciences Division, Lawrence Berkeley National Laboratory, Berkeley, California 94720, USA; and The Raymond and Beverly Sackler Center of Computational Molecular and Materials Science, Tel Aviv University, Tel Aviv 69978, Israel

Ronald Redmer
Institute of Physics, University of Rostock, 18051 Rostock, Germany

Roi Baer
Fritz Haber Research Center for Molecular Dynamics, Institute of Chemistry, The Hebrew University of Jerusalem, Jerusalem 91904, Israel

(Received 24 January 2024; accepted 17 May 2024; published 11 June 2024)

This study overviews and extends a recently developed stochastic finite-temperature Kohn-Sham density functional theory to study warm dense matter using Langevin dynamics, specifically under periodic boundary conditions. The method's algorithmic complexity exhibits nearly linear scaling with system size and is inversely proportional to the temperature. Additionally, a linear-scaling stochastic approach is introduced to assess the Kubo-Greenwood conductivity, demonstrating exceptional stability for dc conductivity. Utilizing the developed tools, we investigate the equation of state, radial distribution, and electronic conductivity of hydrogen at a temperature of 30 000 K. As for the radial distribution functions, we reveal a transition of hydrogen from gaslike to liquidlike behavior as its density exceeds 4 g/cm^3. As for the electronic conductivity as a function of the density, we identified a remarkable isosbestic point at frequencies around 7 eV, which may be an additional signature of a gas-liquid transition in hydrogen at 30 000 K.

DOI: 10.1103/PhysRevE.109.065304

I. INTRODUCTION

Warm dense matter (WDM) exists in the interior of planets [1–10] and in brown dwarf [11–15] and white dwarf stars [16,17]. In inertial and fusion systems [18,19], WDM is generated by subjecting materials to high-energy lasers [20]. Despite its significance, exploring the diverse forms and compositions of WDM poses a formidable challenge due to experimental complexities associated with preparing and sustaining materials under extreme conditions [5,21,22]. Consequently, computational methods have become indispensable for determining the equations of state as well as the chemical and physical properties of different systems.

Among these methods are *ab initio* molecular-dynamics (AIMD) calculations [23–27], which rely on an "adiabatic" approximation. This approximation assumes that the quantum mechanical electrons reach thermal equilibrium under the applied temperature, electronic chemical potential, and Coulomb potentials corresponding to the instantaneous positions of the atomic nuclei. The latter then undergo classical motion under the conservative force derived from the electronic free energy, effectively acting as a potential of mean force (see, e.g., Ref. [28]). The observables can be determined by averaging over a long adiabatic molecular-dynamics (MD) trajectory.

The adiabatic and classical approximations behind AIMD have their limitations. There is evidence suggesting that a classical approximation may lack sufficient accuracy, particularly for temperatures below 1000 K and under high pressures [29,30]. Moreover, nonadiabatic effects, though often disregarded, as done here, have not been thoroughly explored in the context of AIMD in WDM. Previous studies concerning nonadiabatic dynamics on metal surfaces introduce two distinct types of electron-nucleus forces in addition to the adiabatic one [31–34]. The first type manifests as rapid fluctuations resembling a stochastic process, while the second type involves dissipation, simulated as a friction force with a friction constant determined by the electronic structure. Since the molecular dynamics treats atomic nuclei as classical, the Langevin dynamics approach [28,35] can be used to handle

nonadiabatic effects, utilizing fluctuating-dissipating forces to impose the electronic temperature as the average value of the atomic nuclei kinetic energy in a canonical ensemble.

AIMD simulations for WDM need to consider both quantum fermionic degeneracy and strong Coulomb interactions [36]. The Kohn-Sham density functional theory (KS-DFT), which has proven highly successful as an *ab initio* theory for elucidating the structure of molecules and materials at zero temperature [25,37–45], fulfills these requirements and has been extended to finite temperatures, and it has become a widely employed method for theoretical studies of WDM [46–51]. However, applying KS-DFT to WDM requires calculating and storing an increasing number of Kohn-Sham eigenstates as the temperature rises. Consequently, for electronic temperatures exceeding 100 000 K, other approaches, such as the extended KS method [52,53] or "orbital-free DFT," which include finite-temperature orbital free functionals [54–59] and method development [60–66], are preferred. Another emerging approach involves utilizing machine learning to generate potential-energy surfaces and interatomic forces based on KS-DFT and variational quantum Monte Carlo data sets. These learned models can then be employed in molecular-dynamics calculations to predict material properties with reduced computational costs [67–71].

A linear scaling DFT procedure holds significant promise for investigating WDM, whether applied directly in AIMD or for generating training data sets for machine learning. This can be realized through stochastic DFT, as demonstrated by various authors in recent works [72–78]. In this paper, we elaborate on additional advancements in stochastic plane-wave Kohn-Sham density functional theory, integrating it with Langevin dynamics and introducing a novel approach for computing electronic conductivity. We thoroughly assess and benchmark the method, showcasing its practical application by conducting a detailed study of hydrogen at 30 000 K.

II. STOCHASTIC FINITE-TEMPERATURE KOHN-SHAM DFT

A. Finite-temperature Kohn-Sham scheme

The combination of finite-temperature density functional theory [46,79] and the Kohn-Sham procedure (FT-KS-DFT) [80] greatly simplifies the formidable problem of treating interacting electrons under the influence of a heat and electron bath. Under the FT-KS-DFT formalism, we need only study a system of noninteracting electrons in a one-body potential, which includes exchange-correlation contributions. As a result of the exchange-correlation potential, the noninteracting electron density is identical to that of the interacting system, and the grand potential of the interacting electron system can be expressed using the noninteracting grand potential together with exchange-correlation free-energy corrections. As the finite temperature diminishes towards zero, the FT-KS-DFT converges into the zero-temperature KS-DFT, with corresponding exchange-correlation contributions, and the free energy converges to zero-temperature ground-state energy [81].

To study infinite systems, it is beneficial to impose periodic boundary conditions within the simulation cell. The single electron wave functions of the noninteracting system are expressed as a linear combination of the plane-wave basis $e^{i\boldsymbol{G}\cdot\boldsymbol{r}}$:

$$\psi(\boldsymbol{r}) = \sum_{\boldsymbol{G}} \tilde{c}_{\boldsymbol{G}} \frac{e^{i\boldsymbol{G}\cdot\boldsymbol{r}}}{\sqrt{\Omega}}, \tag{1}$$

where $\boldsymbol{G} = \frac{2\pi}{L}(m_x, m_y, m_z)$ is the simulation cell-commensurate wave vector and m_i integers. The wave-vector parameter $G_{\rm cut}$ determines the size of the plane-wave basis by requiring that $\|\boldsymbol{G}\|_2 \leqslant G_{\rm cut}$. This cutoff identifies a subspace of dimension $D = [\frac{3\pi}{4}(\frac{L}{2\pi}G_{\rm cut})^3]$ of the simulation cell's periodic functions, which is mapped by Eq. (1) onto the complex vector space of D-tuples $\mathbb{C}^D = \{\tilde{c}_{\boldsymbol{G}}\}_{\|\boldsymbol{G}\|_2 \leqslant G_{\rm cut}}$. The basis truncation error can be systematically mitigated by increasing $G_{\rm cut}$, or, equivalently, the cutoff energy $E_{\rm cut} = \frac{\hbar^2 G_{\rm cut}^2}{2m_e}$. Variational treatment of the finite-temperature Kohn-Sham equations within the subspace leads to a set of algebraic eigenvalue equations,

$$\mathcal{H}\tilde{c}^{(j)} = \varepsilon_j \tilde{c}^{(j)}, \quad j = 1, 2, \ldots, D, \tag{2}$$

where $\mathcal{H}$ is the Kohn-Sham Hamiltonian (for more details on the representation and the operators, see, for example, Ref. [38]), and ε_j and $\tilde{c}^{(j)}$ are its (real) eigenvalues and (complex) eigenvectors.

The electrons are in a grand-canonical mixed state with temperature parameter $\beta = (k_B T)^{-1}$, where k_B is Boltzmann's constant, and chemical potential μ. The occupation of each single-particle energy level ε is given by the Fermi-Dirac function $p_{\beta\mu}(\varepsilon) \equiv (1 + e^{\beta(\varepsilon-\mu)})^{-1}$. Correspondingly, the electron density can be expressed as a sum of level densities,

$$n(\boldsymbol{r}) = 2 \times \sum_j p_{\beta\mu}(\varepsilon_j)|\varphi_j(\boldsymbol{r})|^2, \tag{3}$$

where

$$\varphi_j(\boldsymbol{r}) = \sum_{\boldsymbol{G}} \tilde{c}_{\boldsymbol{G}}^{(j)} \frac{e^{i\boldsymbol{G}\cdot\boldsymbol{r}}}{\sqrt{\Omega}} \tag{4}$$

are the [normalized, so that $\int_\Omega |\varphi_j(\boldsymbol{r})|^2 d\boldsymbol{r} = 1$] Kohn-Sham eigenstates in real space. The grand potential of the electrons is then given by [82]

$$\Phi_{\beta\mu}[n] \equiv E_{\rm orb} - E_H[n] + \Phi_{\beta\mu,{\rm xc}}[n] - \int v_{\beta\mu,{\rm xc}}(\boldsymbol{r}) n(\boldsymbol{r}) d\boldsymbol{r} - \beta^{-1} S_s[n] - \mu \int n(\boldsymbol{r}) d\boldsymbol{r}, \tag{5}$$

where

$$E_{\rm orb} \equiv 2 \times \sum_j p_{\beta\mu}^j \varepsilon_j \tag{6}$$

is the orbital energy, $p_{\beta\mu}^j = p_{\beta\mu}(\varepsilon_j)$, $E_H[n]$ is the Hartree energy, and $\Phi_{\beta\mu,{\rm xc}}[n]$ is the $\beta\mu$-dependent approximate exchange-correlation free-energy functional of the density, which includes entropy corrections, and $v_{\beta\mu,{\rm xc}}(\boldsymbol{r}) = \frac{\delta\Phi_{\beta\mu,{\rm xc}}}{\delta n(\boldsymbol{r})}$ is the corresponding exchange-correlation potential. Temperature-dependent exchange-correlation free-energy density functionals which have been developed recently [83–89] show that for the temperature ranges and densities

considered in this paper, one can safely use the approximation $\Phi_{\beta\mu,\mathrm{xc}}[n] \approx E_{\mathrm{xc}}^{\mathrm{LDA}}[n]$, where $E_{\mathrm{xc}}^{\mathrm{LDA}}[n]$ is the zero-temperature local-density approximation (LDA, [80]) for the exchange correlation energy, and correspondingly $v_{\beta\mu\mathrm{xc}}(\boldsymbol{r})$ is approximated as the zero-temperature LDA exchange-correlation potential $v_{\mathrm{xc}}^{\mathrm{LDA}}(\boldsymbol{r}) = \frac{\delta E_{\mathrm{xc}}^{\mathrm{LDA}}}{\delta n(\boldsymbol{r})}$. Finally, S_s in Eq. (5) is the entropy of noninteracting electrons at density $n(\boldsymbol{r})$ expressed as

$$S_s = -2 \times k_B \sum_j \left[p_{\beta\mu}^j \log p_{\beta\mu}^j + \bar{p}_{\beta\mu}^j \log \bar{p}_{\beta\mu}^j \right], \tag{7}$$

where, in short, $\bar{p}_{\beta\mu}^j \equiv 1 - p_{\beta\mu}^j$. In this Kohn-Sham procedure, we find the density $n(\boldsymbol{r})$ that minimizes the grand potential $\Phi_{\beta\mu}$. The number of electrons is $\tilde{N}_e(\mu) = (\frac{\partial \Phi_{\beta\mu}}{\partial \mu})_\beta = 2 \times \sum_j p_{\beta\mu}^j$.

The ξ-component ($\xi = 0, 1, 2$ indicates, respectively, x, y, z) of the force on an atomic nucleus $A (A = 0, \ldots, N_n - 1$, where N_n is the number of atomic nuclei in the simulation cell) is equal to the corresponding derivative of the grand potential, $F^i = -\frac{\partial \Phi_{\beta\mu}}{\partial R_i} + F_i^{\mathrm{NN}}$, where $i \equiv (3A + \xi)$ is the force index, and F_i^{NN} is the sum of forces exerted by all other atomic nuclei. This force is an average force over all ground and excited electronic states of all possible charge states of the system.

An alternative to working in the grand-canonical ensemble, where μ is given, is to impose a fixed average number of electrons N_e and then tune μ accordingly. Such an ensemble is more natural for small, finite simulation cells. In this ensemble, the chemical potential becomes a function of the imposed value of N_e, denoted $\tilde{\mu}(N_e)$, defined implicitly by solving the equation

$$N_e = 2 \times \sum_j p_{\beta\tilde{\mu}(N_e)}^j. \tag{8}$$

In this ensemble, we find the density $n(\boldsymbol{r})$ that minimizes the Helmholtz free energy $\mathcal{F}_{\beta N_e} = U - \beta^{-1} S_s$ and the force is its derivative, $F_i = -\frac{\partial \mathcal{F}_{\beta N_e}}{\partial R_i} + F_i^{\mathrm{NN}}$. Once again, this force is an average over all ground and excited electronic states of all possible charge states of the system.

Regardless of the ensemble used, the electronic force component i is obtained from the electron density and the corresponding derivative of the electron-nucleus force potential:

$$F_i = -\int n(\boldsymbol{r}) \frac{\partial}{\partial R_i} v_{\mathrm{eN}}(\boldsymbol{r}) d\boldsymbol{r} + F_i^{\mathrm{NN}},$$

and when nonlocal pseudopotentials are employed, i.e., $\hat{v}_{\mathrm{eN}} = v_{\mathrm{loc}}(\boldsymbol{r}) + \hat{v}_{\mathrm{nl}}$, the following generalization needs to be used (now in vector notation):

$$\boldsymbol{F} = -2 \times \sum_j p_{\beta\mu}^j \langle \varphi_j | \nabla \hat{v}_{\mathrm{eN}} | \varphi_j \rangle + \boldsymbol{F}^{\mathrm{NN}}. \tag{9}$$

B. The stochastic density functional approach

Stochastic density functional theory [72] is based on the concept of random wave functions,

$$\eta(\boldsymbol{r}) \equiv \sum_{\boldsymbol{G}} \tilde{\eta}^{\boldsymbol{G}} \frac{e^{i\boldsymbol{G}\cdot\boldsymbol{r}}}{\sqrt{\Omega}}, \tag{10}$$

in which the random coefficients $\tilde{\eta}^{\boldsymbol{G}}$ are given, in vector notation, by operating with the square-root Fermi-Dirac operator $\sqrt{p_{\beta\mu}(\mathcal{H})}$ on a random vector:

$$\tilde{\eta} \equiv \sqrt{p_{\beta\mu}(\mathcal{H})} \tilde{\chi}, \tag{11}$$

where $\tilde{\chi}$ is a random vector with components $\tilde{\chi}^{\boldsymbol{G}} \equiv e^{i\theta_{\boldsymbol{G}}}$, where $\theta_{\boldsymbol{G}}$ are independent random phases (between 0 and 2π). It is straightforward to check that

$$\mathrm{E}[\tilde{\chi}^{\boldsymbol{G}'} \tilde{\chi}^{\boldsymbol{G}*}] = \delta_{\boldsymbol{G}'\boldsymbol{G}}. \tag{12}$$

Here, the symbol $\mathrm{E}[r]$ is the expected value of a random variable r. The random variable $\tilde{\eta}^{\boldsymbol{G}'} \tilde{\eta}^{\boldsymbol{G}*}$ is an unbiased estimator of the KS density matrix in G-space, relying on the following exact identity: $[p_{\beta\mu}(\mathcal{H})]_{\boldsymbol{G}'\boldsymbol{G}} = \mathrm{E}[\tilde{\eta}^{\boldsymbol{G}'} \tilde{\eta}^{\boldsymbol{G}*}]$. This relation is proved by plugging Eq. (11) on the right-hand side and using Eq. (12). Similarly, sampling $\eta(\boldsymbol{r})\eta(\boldsymbol{r}')^*$, where $\eta(\boldsymbol{r})$ is defined in Eq. (10), provides an estimate for the KS density matrix $\rho(\boldsymbol{r}, \boldsymbol{r}') = 2 \times \sum_j p_{\beta\mu}(\varepsilon_j) \varphi_j(\boldsymbol{r}) \varphi_j(\boldsymbol{r}')^*$. From this, $|\eta(\boldsymbol{r})|^2$ is an unbiased estimator for the electron density $n(\boldsymbol{r})$, relying on the exact identity:

$$n(\boldsymbol{r}) = 2 \times \mathrm{E}[|\eta(\boldsymbol{r})|^2]. \tag{13}$$

This expression is the essence of stochastic KS-DFT: it replaces the *calculation* of the electron density $n(\boldsymbol{r})$ [Eq. (3)], which requires the KS-DFT eigenstates and eigenvalues [Eq. (2)] by a statistical sampling of the random variable $|\eta(\boldsymbol{r})|^2$.

The fact that the expected value of the absolute square of the random variable $\eta(\boldsymbol{r})$ gives the density means that we can now use sampling methods to obtain actual estimates of the density. If we produce a sample of I independent random vectors $\tilde{\chi}_i$ ($i = 1, \ldots, I$), and from them, using Eqs. (10) and (11), obtain samples of $\eta_i(\boldsymbol{r})$, then the density can be estimated as an average

$$n(\boldsymbol{r}) = 2 \times \frac{1}{I} \sum_{i=1}^{I} [|\eta_i(\boldsymbol{r})|^2].$$

This sampling procedure is straightforward to parallelize using a distributed memory model, for example, the message-passing-interface library. Observables such as the forces on atomic nuclei can be expressed as stochastic traces as well (see Sec. III A). From statistics, the fluctuations in the density or forces are proportional to the inverse square root of the sample size. For the calculations shown below, we used a sample of $I = 40$ stochastic orbitals (irrespective of the system size).

C. Chebyshev expansion methods

1. The essential Chebyshev expansion

We now describe a recipe for performing calculations of the type shown in Eq. (11), i.e., operating with a function of the Hamiltonian, namely $z(\mathcal{H})$ on some given a vector χ: $|\zeta\rangle = z(\mathcal{H})|\chi\rangle$. For this, we use the Chebyshev expansion [90] of length N_C, $\zeta^{\boldsymbol{G}} = \sum_{n=0}^{N_C-1} Z^{(n)} \chi_n^{\boldsymbol{G}}$, which we write in ket-form as

$$|\zeta\rangle = \sum_{n=0}^{N_C-1} Z^{(n)} |\chi_n\rangle. \tag{14}$$

The Chebyshev coefficients are defined by

$$Z^{(n)} = \frac{2}{N_C} e^{i\frac{\pi}{N_C}n} \tilde{z}^{(n)},$$

where the series $\{\tilde{z}^{(n)}\}_{n=0}^{N_C-1}$ is the discrete Fourier transform of $\{z[\bar{E} + \Delta E \times \cos(\frac{l+\frac{1}{2}}{N_C}\pi)]\}_{l=0}^{N_C-1}$. In the last expression, $\bar{E} = (E_{\max} + E_{\min})/2$, $\Delta E = (E_{\max} - E_{\min})/2$, and $E_{\min}$ ($E_{\max}$) is a lower (upper) bound estimate to the smallest (largest) eigenvalue of $\mathcal{H}$.

The expansion length N_C is chosen to be sufficiently large so that the $|Z^{(n)}|$ are all smaller than a threshold value 10^{-d} (typically $d = 7$ or 8) for $n > N_C$. An estimate for the Chebyshev length is the following expression:

$$N_C \approx \frac{3d}{4} \times \beta \times \Delta E. \tag{15}$$

The Chebyshev vectors $|\chi_n\rangle$ in Eq. (14) are defined as $|\chi_n\rangle \equiv T_n(\mathcal{H}_s)|\chi\rangle$, where $T_n(x)$ is the nth Chebyshev polynomial [91] and $\mathcal{H}_s \equiv \frac{\mathcal{H}-\bar{E}}{\Delta E}$ is the shifted-scaled Hamiltonian, having all eigenvalues in the interval $[-1, 1]$. Based on a recurrence formula between any three consecutive Chebyshev polynomials [91], the Chebyshev vectors χ_n can be computed iteratively (hence only three of them are needed at a given time):

$$|\chi_n\rangle = 2\mathcal{H}_s|\chi_{n-1}\rangle - |\chi_{n-2}\rangle, \quad n \geqslant 2.$$

The first two vectors are given by

$$|\chi_0\rangle = |\chi\rangle, \qquad |\chi_1\rangle = \mathcal{H}_s|\chi_0\rangle.$$

2. *Operating with several functions of $\mathcal{H}$ on a given state $|\chi\rangle$*

Each term in the Chebyshev expansion of Eq. (14) is a product of a Chebyshev coefficient Z^n and a Chebyshev vector $|\chi_n\rangle$. The former depends on the function $z(\mathcal{H})$, while the latter does not. Suppose we want to operate with several different functions $z_m(\mathcal{H})$ ($m = 1, 2, \ldots, M$) on the *same* vector χ:

$$|\zeta_m\rangle = z_m(\mathcal{H})|\chi\rangle.$$

Chebyshev expansions can calculate these vectors,

$$|\zeta_m\rangle = \sum_{n=0}^{N_C-1} Z_m^{(n)}|\chi_n\rangle, \tag{16}$$

where $Z_m^{(1)}, Z_m^{(2)}, \ldots$ are the coefficients corresponding to the function $z_m(\varepsilon)$. Most of the numerical effort goes into computing the vectors $|\chi_n\rangle$, and these are shared by all the different evaluations in Eq. (16). Therefore, there is only a minute overhead in the effort to calculate M $|\zeta_m\rangle$'s relative to just one $|\zeta\rangle$.

3. *Energy windows*

An example of using this approach is the *Energy Windows* method [92]. Here, we define N_w chemical potentials,

$$\mu_{N_w} \equiv \mu \geqslant \mu_{N_w-1} \geqslant \cdots \geqslant \mu_1,$$

and corresponding energy window projections,

$$z_m(\mathcal{H}) = \sqrt{p_{\beta\mu_m} - p_{\beta\mu_{m-1}}}, \qquad m = 2, \ldots, N_w,$$
$$z_1(\mathcal{H}) = \sqrt{p_{\beta\mu_1}}.$$

Each of these functions projects a different energy range between the chemical potentials. The sum of the square of these functions yields the Fermi-Dirac projector

$$p_{\beta\mu}(\mathcal{H}) = z_{N_w}(\mathcal{H})^2 + z_{N_w-1}(\mathcal{H})^2 + \cdots + z_1(\mathcal{H})^2.$$

Therefore, for any one-body operator $\mathcal{A}$, the KS expectation value $\langle\mathcal{A}\rangle \equiv \mathrm{Tr}[p_{\beta\mu}(\mathcal{H})A]$ can be written as a sum of contributions from differing energy windows:

$$\langle\mathcal{A}\rangle = \sum_{m=1}^{N_w} \mathrm{Tr}[z_m(\mathcal{H})Az_m(\mathcal{H})].$$

The equivalent stochastic expression is

$$\langle\mathcal{A}\rangle = \sum_{m=1}^{N_w} \mathrm{E}[\langle\zeta_m|\mathcal{A}|\zeta_m\rangle].$$

Depending on the observable $\mathcal{A}$, this procedure helps reduce the fluctuations in estimating $\langle\mathcal{A}\rangle$ since ζ_m and $\zeta_{m'}$ span largely nonoverlapping energy windows.

In the left panel of Fig. 1, we show the standard deviation of the electronic force on the atomic nuclei (per degree of freedom) as a function of the number of windows for selected temperatures. It is seen that for low temperatures this standard deviation is reduced by as much as a factor of 2 as N_W reaches 16 or 32. However, for the high temperature considered, the windows are less efficient, reducing the standard deviation by, at most, a factor of 1.4.

4. *Chebyshev moments*

A Chebyshev moment M_n is the *trace* of a Chebyshev polynomial $T_n(\mathcal{H}_s)$. The overlap $\langle\chi|\chi_n\rangle$ is an unbiased estimator of M_n, based on the identity $\mathrm{Tr}[T_n(\mathcal{H}_s)] = \mathrm{E}[\langle\chi|T_n(\mathcal{H}_s)|\chi\rangle]$, or

$$M_n = \mathrm{E}[\langle\chi|\chi_n\rangle].$$

Knowledge of the moments allows us to compute the trace of any function $z(\mathcal{H})$ of the KS Hamiltonian $\mathcal{H}$ through the formula

$$\mathrm{Tr}[z(\mathcal{H})] = \sum_{n=0}^{N_C-1} Z^{(n)}M_n,$$

where $Z^{(n)}$ are the coefficients for the Chebyshev expansion of the function $z(\varepsilon)$.

The following examples show where moments are useful:

(i) When working in the canonical ensemble mentioned above, with a fixed number of electrons N_e, the chemical potential μ is a function of N_e defined implicitly by Eq. (8), depending on the KS eigenvalues ε_j. However, in sDFT, we do not have access to ε_j. Hence, we use the Chebyshev moments to develop an alternative implicit equation for μ:

$$N_e = 2 \times \sum_{n=0}^{N_C-1} P_{\beta\mu(N_e)}^{(n)} M_n, \tag{17}$$

where the $P_{\beta\mu}^{(n)}$'s are the Chebyshev coefficients corresponding to $p_{\beta\mu}(\varepsilon)$. The actual determination of μ uses a numerical root-searching algorithm (e.g., the bisection method) applied to Eq. (17). The search for μ is a speedy step since the Chebyshev moments are independent of μ, so they are calculated

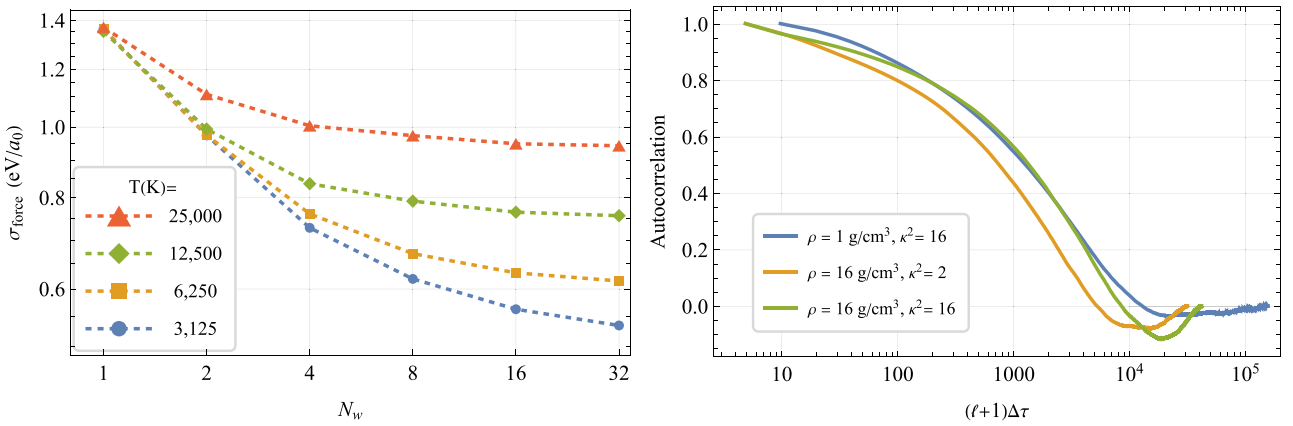

FIG. 1. Left panel: The sDFT force standard deviation $\sigma_f \equiv \sqrt{\frac{1}{3N_H}\text{Tr}\Sigma_\phi^2}$ (per degree of freedom) for selected electronic temperatures as a function of the number of windows N_w in H_{128} at $\rho = 1$ g/cm^3. Right panel: The instantaneous position autocorrelation $C_R(\ell)$ [see Eq. (24), averaged over all atoms] during a $T = 30\,000$ K Langevin trajectory of H_{256} in two densities with additional white noise force [given in terms of κ, see Eq. (22)] and a time step of $\Delta t = 5\,\hbar E_h^{-1}$ for $\rho = 16$ g/cm^3 and $\Delta t = 10\,\hbar E_h^{-1}$ for $\rho = 1$ g/cm^3.

only once and then stored, while calculating the Chebyshev coefficients $P_{\beta\mu}$ for any value of μ only involves a single fast Fourier transform.

(ii) The noninteracting electron entropy of Eq. (7) is estimated as

$$S_s = 2 \times \sum_{n=0}^{N_C-1} S_{\beta\mu}^{(n)} M_n, \tag{18}$$

where $S_{\beta\mu}^{(n)}$ are the Chebyshev coefficients corresponding to the function $s_{\beta\mu}(\varepsilon) = -[p_{\beta\mu}(\varepsilon)\log p_{\beta\mu}(\varepsilon) + \bar{p}_{\beta\mu}(\varepsilon)\log \bar{p}_{\beta\mu}(\varepsilon)]$.

(iii) The orbital energy E_{orb} of Eq. (6) is estimated as

$$E_{\text{orb}} = 2 \times \sum_{n=0}^{N_C-1} E_{\beta\mu}^{(n)} M_n,$$

where the $E_{\beta\mu}^{(n)}$ are the Chebyshev coefficients corresponding to $e_{\beta\mu}(\varepsilon) = p_{\beta\mu}(\varepsilon)\varepsilon$.

D. Performance of the sDFT calculation

Figure 2 shows the wall time self-consistent calculations (averaged over many sDFT Langevin dynamics steps) as a function of the number of electrons N_e in the simulation cell for hydrogen at specified densities and temperatures. The computation time of a single cycle of an SCF calculation scales linearly in $x = N_e \log N_e$. Since the number of SCF cycles required to converge to a given criterion grows mildly with system size, the overall scaling is $x^{1.3}$. Calculations with higher temperatures and the same number of electrons N_e are faster since the Chebyshev expansions shorten in inverse proportion to temperature [see Eq. (15)]. Higher density calculations with the same number of atoms N_e also require less computation time because of the smaller simulation cell sizes.

Let us discuss the wall times and their dependence on scale for the cutoff energy E_{cut}. The plane-wave basis size is determined by the volume in G-space of the highest momentum vector $G_{\max} = \sqrt{\frac{2m_e}{\hbar^2}E_{\text{cut}}}$ (where m_e is the electron mass and $\hbar$ is Planck's constant) and is therefore proportional to $E_{\text{cut}}^{3/2}$. In addition, the length of the Chebyshev expansion is proportional to E_{cut} [see Eq. (15)]. Hence, overall, the wall time scales steeply as $E_{\text{cut}}^{5/2}$, i.e., wall time increases by a factor 32 every time the cutoff energy increases by a factor 4.

We have not yet developed the capability to expedite the calculation speed for each stochastic orbital. We can achieve high factors if we use a GPU on each node for this purpose.

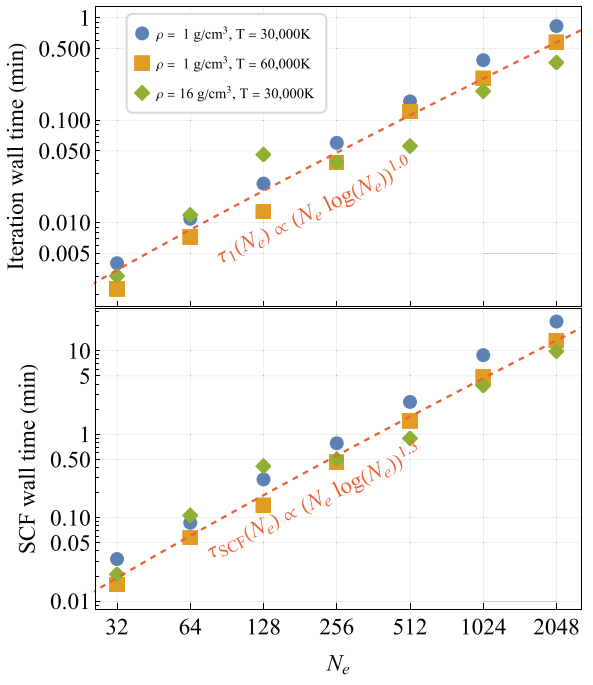

FIG. 2. The self-consistent-field (SCF) wall times as a function of the number of electrons N_e for hydrogen at the specified densities and temperatures. Top panel: a single SCF iteration; bottom panel: the entire SCF calculation (stopped when the changes in energy per electron are below 10^{-5}E$_h$). The calculations used the cutoff energy of $E_{\text{cut}} = 9$ E$_h$, 40 stochastic orbitals, and a *single core per stochastic orbital* on our Core-i7 cluster.

III. STOCHASTIC FORCES AND LANGEVIN DYNAMICS

In the previous section, we discussed the WDM's electronic structure at inverse temperature β. In this section, we concentrate more on the behavior of the atomic nuclei in WDM. At thermal equilibrium their state is canonically distributed with a temperature identical to that of the electrons. Here we discuss how we use the method of Langevin dynamics to estimate the expected value of various observables concerning atomic nuclei within the canonical ensemble.

A. Regularization of the stochastic forces

In sDFT, the force on each atomic nucleus is a vector of a random variable components [72]:

$$\boldsymbol{f} = -2 \times \langle \eta | \nabla \hat{v}_{\mathrm{eN}} | \eta \rangle + \boldsymbol{F}^{\mathrm{NN}}, \tag{19}$$

where $\eta(\boldsymbol{r})$ is defined in Eq. (10), and $\boldsymbol{F}^{\mathrm{NN}}$ is the force due to the other bare atomic nuclei. Using the stochastic trace formula, the force $\boldsymbol{F}$ of Eq. (9) is the expected value of the random force:

$$\boldsymbol{F} = \mathrm{E}[\boldsymbol{f}].$$

The $3N_n \times 3N_n$ symmetric positive-definite force covariance matrix is $(\Sigma_f^2)_{ii'} = \mathrm{E}[f_i f_{i'}] - F_i F_{i'}$, or, in matrix notation,

$$\Sigma_f^2 \equiv \mathrm{E}[\boldsymbol{f}\boldsymbol{f}^T] - \boldsymbol{F}\boldsymbol{F}^T. \tag{20}$$

To ease the handling of stochastic forces, we add independent white noise $\boldsymbol{\zeta}$ ($\mathrm{E}[\boldsymbol{\zeta}] = 0$):

$$\boldsymbol{\varphi} = \boldsymbol{f} + \boldsymbol{\zeta}. \tag{21}$$

The covariance matrix $\mathrm{E}[\boldsymbol{\zeta}\boldsymbol{\zeta}^T]$ of this additional white noise is specially constructed to allow the covariance $\Sigma_{\boldsymbol{\varphi}}^2$ of the total force to be uniform, i.e., a *multiple of the unit matrix*:

$$\Sigma_{\boldsymbol{\varphi}}^2 \equiv \mathrm{E}[\boldsymbol{\varphi}\boldsymbol{\varphi}^T] - \boldsymbol{F}\boldsymbol{F}^T = \sigma^2 \mathrm{I} = \kappa^2 \sigma_f^2 \mathrm{I}, \tag{22}$$

where σ^2 is larger ($\kappa \geqslant 1$) than the largest eigenvalue σ_f^2 of Σ_f^2. The white noise force ζ is thus sampled, using the Metropolis-Hastings algorithm, to have a Gaussian distribution with the positive-definite covariance matrix $\Sigma_\zeta^2 \equiv \sigma^2 I - \Sigma_f^2$. The procedure obviously requires an estimate of the sDFT force covariance Σ_f^2 and we use a sample of N_s force vectors to estimate it (with $N_s = 50$, seemingly quite sufficient). The covariance estimate is done once every N_j MD step (we took $N_j = 150$). A force having such a uniform covariance matrix enables using the same friction coefficient for all degrees of freedom, and therefore simplifies the temperature control in the Langevin dynamics calculation.

B. Stochastic Langevin equations of motion

The stochastic force $\boldsymbol{\varphi}(\boldsymbol{R})$ for a given atomic nuclei configuration is now used to perform Langevin molecular dynamics from which we obtain configuration and momentum samples that are canonically distributed. From these samples we can compute the thermodynamic properties of the system. The dynamics involves solving the Langevin equation of motion

$$\dot{\boldsymbol{P}}(t) = \boldsymbol{\varphi}(\boldsymbol{R}(t)) - \gamma \boldsymbol{P}(t),$$
$$\dot{\boldsymbol{R}}(t) = M^{-1}\boldsymbol{P}(t),$$

where M^{-1} is a diagonal matrix of the inverse nuclei mass, and γ is the diagonal matrix of friction coefficients. We use a time-discretized solver [93] for the stochastic differential equation, from which we obtain a discretized trajectory of N_T atomic configurations $\boldsymbol{R}^{(n)} = \boldsymbol{R}(n\Delta\tau)$ $(n = 1, \ldots, N_T)$ and their momenta $\boldsymbol{P}^{(n)} = \boldsymbol{P}[(n - \frac{1}{2})\Delta\tau]$, where $\Delta\tau$ is the time step. The phase-space trajectory is built from the following evolution steps:

$$\boldsymbol{P}^{(n+1)} = e^{-\gamma\Delta\tau}\boldsymbol{P}^{(n)} + \left(\frac{1 - e^{-\gamma\Delta\tau}}{\gamma}\right)\boldsymbol{\varphi}(\boldsymbol{R}^{(n)}),$$
$$\boldsymbol{R}^{(n+1)} = \boldsymbol{R}^{(n)} + M^{-1}\boldsymbol{P}^{(n+1)}\Delta\tau,$$

and in the limit $\Delta\tau \to 0$ a Langevin trajectory is obtained. Here, the (diagonal) friction matrix γ is determined from the fluctuation-dissipation relation, which is given by

$$\sigma^2 = \frac{\gamma\Delta\tau/2}{\tanh(\gamma\Delta\tau/2)} \times \frac{2\gamma M}{\beta}. \tag{23}$$

C. Statistical sampling

For sufficiently small $\Delta\tau$, each of the trajectory configurations $\boldsymbol{R}^{(n)}$ is equivalent to a sample taken from the Boltzmann distribution $p_\beta^B(\boldsymbol{R}) \propto e^{-\beta V_{\mathrm{BO}}(\boldsymbol{R})}$, where $V_{\mathrm{BO}} \equiv \Phi_{\beta\mu} + E_{\mathrm{NN}}$ ($V_{\mathrm{BO}} = \mathcal{F}_{\beta N_e} + E_{\mathrm{NN}}$) is the *electronic* grand-canonical (canonical) potential [see Eq. (5)]. The momentum $\boldsymbol{P}^{(n)}$ is equivalent to a sample from the Maxwell-Boltzmann probability distribution function $p_{R\beta}^{\mathrm{MB}}(\boldsymbol{P}) \propto e^{-\beta\sum_{i=1}^{N_N}\frac{P_i^2}{2M_i}}$.

The estimate for the thermal average $\langle O \rangle_\beta \equiv \iint O(\boldsymbol{R},\boldsymbol{P}) p_\beta^B(\boldsymbol{R}) d\boldsymbol{R} p_\beta^{MB}(\boldsymbol{P}) d\boldsymbol{P}$ of a given observable $O(\boldsymbol{R},\boldsymbol{P})$ is simply the sample mean $\bar{O} \equiv \frac{1}{N_T}\sum_{n=1}^{N_T} O^{(n)}$ over the sequence $O^{(n)} \equiv O(\boldsymbol{R}^{(n)}, \boldsymbol{P}^{(n)})$. The sample variance $\overline{\Delta O^2} = \frac{1}{N_T}\sum_{n=1}^{N_T}\Delta O^{(n)}$, where $\Delta O^{(n)} = O^{(n)} - \bar{O}$, allows us to determine a confidence interval for the thermal average. For example, the 70% confidence interval is $[\bar{O} - \delta O, \bar{O} + \delta O]$, where $\delta O \equiv \sqrt{\frac{1}{N_{\mathrm{ind}}}\overline{\Delta O^2}}$ and N_{ind} is the number of statistically independent samples in the sequence $O^{(n)}$. If the values $O^{(1)}, O^{(2)}, \ldots$ were uncorrelated, then N_{ind} would be just the sample size N_T. However, because the configurations $\boldsymbol{R}^{(n)}$ are part of a *molecular-dynamics trajectory*, $O^{(n+1)}$ is *correlated* with $O^{(n)}$, and $O^{(n+2)}$ is correlated with $O^{(n+1)}$, etc., and therefore $N_{\mathrm{ind}} < N_T$. It is common to quantify the strength of this correlation using *the autocorrelation function* for O, defined by $C_O(\ell\Delta\tau) \equiv \frac{\langle \Delta O^{(n)}\Delta O^{(n+\ell)}\rangle}{\langle \Delta O^{(n)2}\rangle}$ (the expression on the right-hand side is independent of n). In a given sample trajectory, the autocorrelation function is estimated by

$$C_O(\ell\Delta\tau) \approx \frac{\sum_n \Delta O^{(n)}\Delta O^{(n+\ell)}}{\sum_n \Delta O^{(n)2}}. \tag{24}$$

It starts with the value $C_O(0) = 1$ (full correlation) and then decays steadily as step separation ℓ grows until hitting a regime of small random fluctuations. The decay is characterized by a correlation time τ_O, for which $C_O(\tau_O) = e^{-1}$.

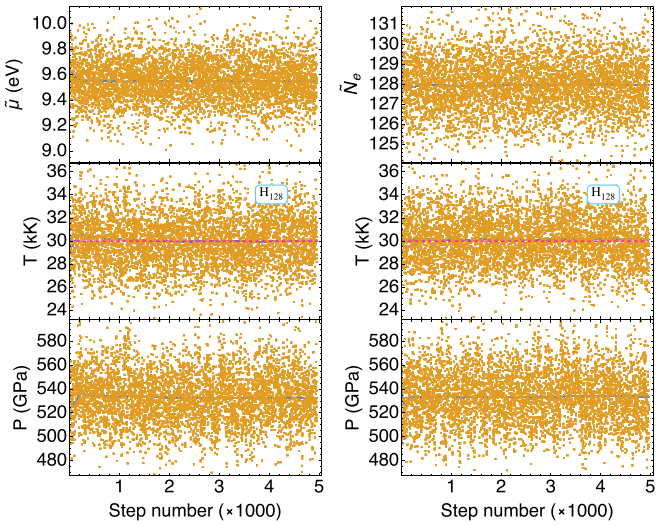

FIG. 3. The instantaneous values (brown) and running averages (blue) of observables in two Langevin molecular-dynamics trajectories of H_{128} (at a mass density of $\rho = 1\,\mathrm{g/cm^{-3}}$ and a target temperature of 30 000 K). Left panel: the NVT-like trajectory, where the number of electrons is fixed ($N_e = 128$) by tuning the chemical potential $\tilde{\mu}^{(n)}$ at each time step [see Eq. (8)]. Right panel: the μVT trajectory, where the chemical potential is fixed ($\mu = 9.56$ eV) while the number of electrons $N_e^{(n)}$ fluctuates. Details of the Langevin dynamics: the white noise fluctuation is $\sigma = 4\sigma_f$, i.e., $\kappa = 4$ [see Eq. (22)], the time step is $\Delta\tau = 10$ atu, and the sDFT force covariance [see Eq. (20)] is calculated using 50 independent samples once every 150 dynamical time steps.

We also define the *correlation length* $\ell_O = \frac{\tau_O}{\Delta\tau}$. We view ℓ_O consecutive samples as "correlated" while later samples are considered *uncorrelated*. The number of *effectively independent* samples is thus estimated as $N_{\mathrm{ind}} \approx N_T/\ell_O$. In the right panel of Fig. 1 we show the Langevin dynamics position autocorrelation function $C_R(\ell\Delta\tau)$ of hydrogen at $T = 30\,000$ K, for two densities ρ and two white noise parameters κ^2 [see Eq. (22)]. The correlation times τ_R are weakly dependent on the density but grow significantly with κ. Hence, we strive for small values of $\kappa^2 > 1$.

D. Computational demonstration of μVT-N_eVT ensemble equivalence

Figure 3 displays time-dependent values of selected observables in two Langevin dynamics trajectories of hydrogen at mass density $\rho = 1\,\mathrm{g/cm^{-3}}$ at $T = 30\,000$ K. The two trajectories are calculated in different electronic ensembles: the left panel of the plot shows the results of an N_eVT-like ensemble, where we impose a constant electron number $N_e = 128$ at each time step by tuning the electronic chemical potential $\tilde{\mu}(N_e; \boldsymbol{R}^{(n)})$ in the Fermi-Dirac function at each time step [see Eq. (8)]. This chemical potential fluctuates in time, as do the positions and momenta of the atomic nuclei. The right panel shows the results of an μVT ensemble, where the electronic chemical potential is set to a constant value of $\mu = 9.56$ eV. Now the number of electrons fluctuates, but *on average* it is 128. The observables are the kinetic energy per atomic degree of freedom $T^{(n)}$ (divided by k_B and given in 10^3 Kelvin), the pressure $P^{(n)}$, the chemical potential $\tilde{\mu}^{(n)}$, and the Helmholtz energy $\tilde{\mathcal{F}}^{(n)}_{\beta N_e}$ in the left panel, and the electron number $\tilde{N}_e^{(n)}$ and the grand potential $\tilde{\Phi}^{(n)}_{\beta\mu}$ in the right panel. Upon studying the numerical results in Fig. 3, it is obvious that the average over the fluctuating chemical potential in the left panel $\langle\tilde{\mu}\rangle_{N_eVT} = \frac{1}{N_T}\sum_{n=1}^{N_T}\tilde{\mu}(N_e; \boldsymbol{R}^{(n)})$ is very similar to the constant chemical potential μ imposed in the μVT ensemble in the right panel. Similarly, the average over the fluctuating number of electrons in the right panel $\langle\tilde{N}_e\rangle_{\mu VT} = \frac{1}{N_T}\sum_{n=1}^{N_T}\tilde{N}_e(\mu; \boldsymbol{R}^{(n)})$ is very close to the imposed number of electrons N_e used in the N_eVT ensemble in the left panel. These results can be summarized in the following relation:

$$\mu = \langle\tilde{\mu}\rangle_{N_eVT} \Leftrightarrow N_e = \langle\tilde{N}_e\rangle_{\mu VT},$$

showing that in our finite-sized system, the two ensembles μVT and N_eVT are already equivalent, which is characteristic of the thermodynamic limit. All calculations shown in the next section were performed in the N_eVT ensemble.

IV. KUBO-GREENWOOD CONDUCTIVITY

In this section, we consider the stochastic calculation of the Kubo-Greenwood conductivity [94,95]. In the context of WDM, these calculations were addressed in Refs. [96,97] but they become demanding as the system size and temperature increase. Hence, a stochastic calculation may be preferable for such systems as discussed in Ref. [74]. Here, we provide an improved approach including the dc conductivity with considerably lower statistical errors. We also provide a detailed description of the theory, the derivation, and how the calculations were made.

Kubo's analysis [94] starts with expressing the complex conductivity,

$$\sigma_{\xi\xi'}(\omega) = \int_0^\infty \phi_{\xi\xi'}(t)e^{-i\omega t}dt, \tag{25}$$

as the Fourier transform of the dipole-current-density response function:

$$\phi_{\xi\xi'}(t) = \frac{1}{i\hbar}\mathrm{tr}\left(\rho\left[\sum_n e\mathcal{R}_{n\xi}, \sum_{n'}\frac{e\mathcal{V}_{n'\xi'}(t)}{\Omega}\right]\right),$$

where e is the electron charge, tr is a many-body trace, ρ is the equilibrium (many-body) density matrix, $\mathcal{R}_{n\xi}$ is the position in Cartesian direction ξ ($\xi = x, y, z$) of electron n, and $\mathcal{V}_{n\xi} \equiv \frac{\hbar}{m_e}(\frac{1}{i}\frac{\partial}{\partial\mathcal{R}_{n\xi}} - k_\xi)$ is the corresponding velocity (where $k_\xi = \frac{\pi}{2L_\xi}$ is the Baldereschi k-point). For noninteracting electrons, the response function reduces to a single electron expression (see Appendix A):

$$\phi_{\xi\xi'}(t) = \frac{4e^2}{\hbar\Omega}\mathrm{Im}\,\mathrm{Tr}(p_{\mu\beta}(\mathcal{H})\mathcal{R}_\xi\mathcal{V}_{\xi'}(t)), \tag{26}$$

where Tr is a single-particle operator trace, $\mathcal{R}_\xi$ and $\mathcal{V}_{\xi'}$ are single electron position and velocity operators, respectively, $p_{\mu\beta}(\mathcal{H})$ is the Fermi-Dirac distribution, and $\mathcal{H}$ is the single-particle Hamiltonian (at the Baldereschi k-point), which we take from KS-DFT. We have also included a factor 2 due to spin-degeneracy. The use of such a static KS Hamiltonian, as opposed to the TDDFT description, is the central approximation of the Kubo-Greenwood theory.

For $\omega \neq 0$, we multiply and divide by $-i\omega$ the integral of Eq. (25), use the identity $-i\omega e^{-i\omega t} = \frac{d}{dt}e^{-i\omega t}$, and then integrate by parts, obtaining

$$\sigma_{\xi\xi'}(\omega) = \frac{1}{i\omega}\left(-\phi_{\xi\xi'}(0) + \int_0^\infty \dot{\phi}_{\xi\xi'}(t)e^{-i\omega t}dt\right), \tag{27}$$

which involves the velocity-velocity response function:

$$\dot{\phi}_{\xi\xi'}(t) = -\frac{4e^2}{\hbar\Omega}\mathrm{Im}\,\mathrm{Tr}(p_{\mu\beta}(H)\mathcal{V}_\xi\mathcal{V}_{\xi'}(t)).$$

For evaluating the trace, we use the stochastic trace formula:

$$\mathrm{Tr}(p\mathcal{V}_\xi\mathcal{V}_{\xi'}(t)) = \mathbb{E}[\langle\zeta_{\xi t}|\mathcal{V}_{\xi'}|\eta_t\rangle], \tag{28}$$

where, for brevity, $p = p_{\beta\mu}(\mathcal{H})$ and

$$|\eta_t\rangle \equiv e^{-i\mathcal{H}t/\hbar}\sqrt{p}|\chi\rangle, \quad |\zeta_{\xi t}\rangle \equiv e^{-i\mathcal{H}t/\hbar}\mathcal{V}_\xi|\eta\rangle,$$

and $|\chi\rangle$ is a stochastic state. To use Eq. (28) we generate a sample of N_s stochastic vectors χ, and for each, we obtain a specific value of $\langle\zeta_{\xi t}|\mathcal{V}_{\xi'}|\eta_t\rangle$. Averaging these values gives an estimate of the trace in the response function with a statistical error proportional to $1/\sqrt{N_s}$.

The trace operations provide correlation functions, which we denote $\dot{\phi}(t)$ [whether $\dot{\phi}_{\xi\xi'}(t)$ described above or $\dot{\psi}_{\xi\xi'}(t)$ described below]. To use it for obtaining the conductivity as a function of ω, we first select a desired spectral energy resolution $\hbar\nu$, which defines a frequency grid $\omega_g = g \times \nu$, where $g = 0, 1, \ldots, N_\omega$, and then we perform the Fourier integral of Eq. (27) for these frequencies. Given the resolution, the integral of the correlation function $\dot{\phi}(t)$ is augmented by a Gaussian window, discretized, and summed utilizing the fast-Fourier algorithm

$$\begin{aligned}\int_0^\infty \dot{\phi}(t)e^{-i\omega_g t}dt &\to \int_0^\infty e^{-\frac{\nu^2 t^2}{2}}\dot{\phi}(t)e^{-i\omega_g t}dt \\ &\to \frac{\tau_f}{N_\omega}\sum_{g'=0}^{N_\omega} w_{g'}e^{-\frac{\nu^2\tau_{g'}^2}{2}}\dot{\phi}(\tau_{g'})e^{-i\omega_g\tau_{g'}}\end{aligned} \tag{29}$$

on an equally spaced time-grid $\tau_g = g \times \frac{\tau_f}{N_\omega}$, extending from zero to $\tau_f = 7/\nu$. The number of time and frequency grid points is taken as $N_\omega = q_{\mathrm{fac}} \times \frac{E_{\mathrm{cut}}}{\hbar\nu}$, where the quality factor $q_{\mathrm{fac}} > 1$ determines the precision of the time integration. We also inserted integration weights, the simplest of which is the trapeze rule: $w_k = (1 - \delta_{k0}/2)$. These weights are essential as the integral is a half-Fourier transform, which means that the integrand does not decay smoothly to zero at the time-grid boundaries. We experimented with various choices of ν and q_{fac}, finding that a resolution of $\hbar\nu = 0.025$ $\mathrm{E_h}$ and a quality factor in the range of 3–5 yield meaningful and stable results. Dividing these values by $i\omega_g$ ($g > 0$), we obtain the ac conductivity $\sigma_{\xi\xi'}(\omega_g)$.

Since evaluating the conductivity in Eq. (27) requires division of the Fourier integral by ω, the statistical fluctuations are amplified as $\omega \to 0$. The procedure is undefined for $\omega = 0$, the dc limit. In this case, we could use the analytical limit of Eq. (27),

$$\mathrm{Re}\sigma_{\xi\xi'}(0) = \int_0^\infty \dot{\phi}_{\xi\xi'}(t)t\,dt, \tag{30}$$

which does not divide by zero. We can use the same integration procedure outlined above for the integral. But experience shows that the stochastic error in Eq. (30), although finite, is not small and requires extensive sampling. For the important case of $\xi = \xi'$, it is possible to show (see Appendix B) that

$$\mathrm{Re}\sigma_{\xi\xi}(0) = \int_0^\infty \dot{\psi}_{\xi\xi}(t)dt, \tag{31}$$

where [see Eq. (B4)]

$$\dot{\psi}_{\xi\xi}(t) = -\frac{2e^2}{\Omega}\,\mathrm{Re}\,\mathrm{Tr}(p'_{\mu\beta}(H)\mathcal{V}_\xi\mathcal{V}_\xi(t)),$$

and $p'_{\mu\beta}(\varepsilon) = -\beta p_{\mu\beta}(\varepsilon)[1 - p_{\mu\beta}(\varepsilon)]$ is the derivative of the Fermi-Dirac function. The stochastic evaluation of the correlation function $\mathrm{Tr}(p'_{\mu\beta}(H)\mathcal{V}_\xi\mathcal{V}_\xi(t))$ follows the same procedure as $\mathrm{Tr}(p_{\mu\beta}(H)\mathcal{V}_\xi\mathcal{V}_\xi(t))$ except that this time we take $p = p'_{\beta\mu}(\mathcal{H})$. Then, the same time-integration scheme outlined above for the Fourier integral of $\dot{\phi}_{\xi\xi}$ can be used to evaluate the integral of Eq. (31).

The problem of high fluctuations in the low-frequency part of the ac conductivity is exacerbated due to the need to take smaller ν for converging the ac results to the dc limit: the smaller ν is, the larger are the fluctuations. Thus, we developed an interpolation procedure for the low-frequency spectrum relying on the steadiness of the dc conductivity. This procedure is described in Appendix C.

For calculating the direction-averaged conductivity, $\bar{\sigma} = \frac{1}{3}(\sigma_{xx} + \sigma_{yy} + \sigma_{zz})$, we replace the ξ component of the velocity ($\mathcal{V}_\xi$) in the above equations by a random-direction component $\mathcal{V}_d = \boldsymbol{\eta}^T\boldsymbol{V}$, where $\boldsymbol{\eta} = (\eta_x, \eta_y, \eta_z)$, taken as a *random point* on the 3D unit sphere, since $\mathbb{E}[\boldsymbol{\eta}\boldsymbol{\eta}^T] = \frac{1}{3}\mathcal{I}$, where $\mathcal{I}$ is the 3×3 unit matrix. Averaging over $\mathcal{V}_d$ automatically computes $\bar{\sigma}$.

V. TEST CASE: HYDROGEN AT 30 000 K

In this section, we use as a test case hydrogen at 30 000 K. We first consider system-size effects on the estimation of pressure and conductivity. Then, we give its equation of state, electric conductivity, and radial distributions, comparing, where possible, with VASP [98–102].

All sDFT calculations in this section used 40 stochastic orbitals (for all system sizes), the LDA exchange-correlation energy functional, and norm-conserving pseudopotentials [103]. Unless specifically mentioned otherwise, we use 9 $\mathrm{E_h}$ cutoff energy and the Baldereschi k-point [104].

A. System-size-dependent pressure and conductivity

In Fig. 4 we present the pressure (left panel) and the conductivity (right panel) estimates for hydrogen at 30 000 K and density $\rho = 1$ g/cm^3, as a function of the system size. The pressure estimates at the Baldereschi k-point are rather steady and change only mildly with system size. Those done at the Γ point show a stronger sensitivity to system size, peaking at H_{256} and then decreasing towards the steadier k-point values. The sDFT pressure estimates increase by about 5% when going from cutoff energy of 9 to 25 $\mathrm{E_h}$. The dDFT results, based on the VASP code, are less sensitive to the cutoff energy and change by only 2.5%. This reflects the superiority of the PAWs

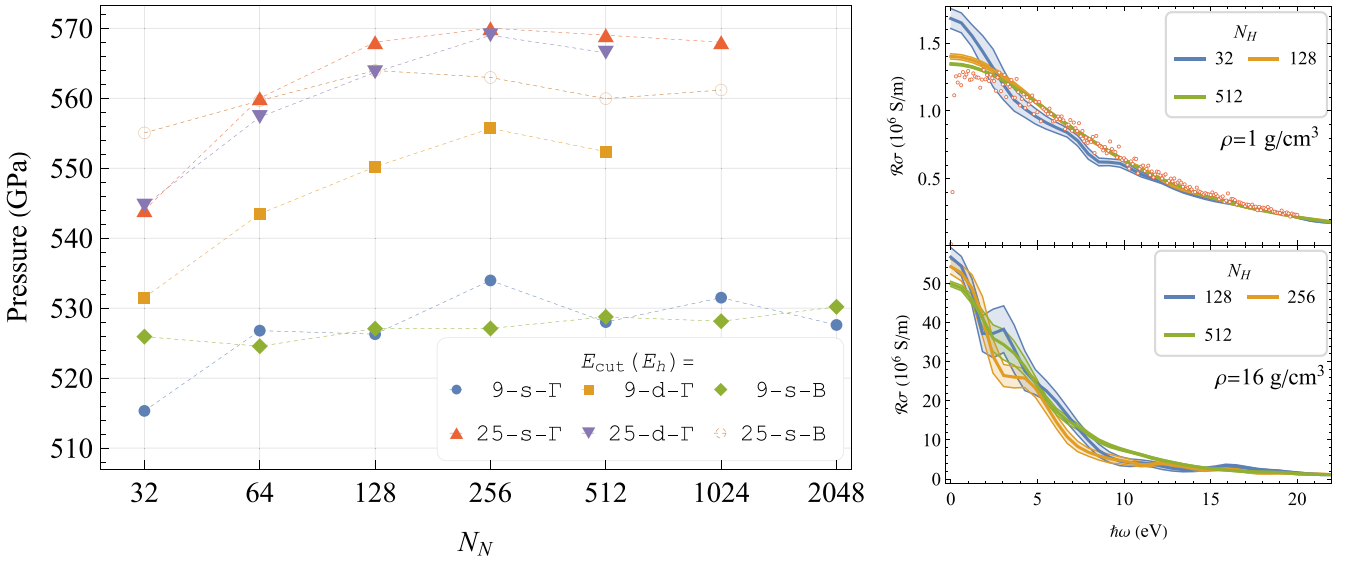

FIG. 4. Pressure and conductivity averaged over a Langevin trajectory. Left panel: Size dependence of pressure at density 1 g/cm^3. Each point on the graph is an average over the pressure estimates along the xDFT (x="s" or "d") trajectory, performed using 9 or 25 E_h cutoff energy at the Γ or B (Baldereschi) k-point, as indicated in the legend. The sDFT calculations for each point on the Langevin trajectory used 40 stochastic orbitals at the LDA/NCPPs level. The dDFT calculations were performed by the VASP program [98–102], at the LDA/PAW level. The trajectory time step was $\Delta\tau = 5$ atu, and white noise parameter $\kappa^2 = 2$. Right panels: Size dependence of the conductivity where the top (bottom) panel shows results for $\rho = 1(16)$ g/cm^3. Each conductivity curve is an average over the conductivity curves calculated for $N_s = 20$ configurations of the atomic nuclei (snapshots) taken every 1000 atu along the sDFT/Langevin trajectory. The error bars are $\pm s/\sqrt{N_s}$, where s is the standard deviation. One conductivity calculation produces an entire conductivity curve [$\sigma(\omega)$] based on 120 stochastic orbitals, performed at the Baldereschi k-point, with a 15 E_h cutoff energy. Dark empty circles appearing in the top-right panel are conductivity calculations for H_{128} on the identical configurations using the deterministic conductivity method of Ref. [96] using VASP.

used by VASP over the norm-conserving pseudopotentials used in the sDFT calculation when converging to the infinite energy cutoff limit. The sDFT and the VASP pressure estimates are similar at the higher cutoff energy.

The size dependence of hydrogen conductivity at 30 000 K, calculated at the Baldereschi k-point, is shown for two density values in the right panel of Fig. 4. For 1 g/cm^3, the conductivity curves of H_{128} and H_{512} are already quite close (a difference of 3%). Note that the larger the system, the smaller the fluctuations. We also show results from a deterministic calculation on H_{128}, which tend to be too small as ω decreases but fit our results well for all other frequencies.

Finally, the conductivity for the high-density systems is much more noisy than at low density, and the system size effects are more noticeable, since the simulation cell size is small for these systems.

B. Density-dependent properties of hydrogen at 30 000 K

The estimated pressure of hydrogen at $T = 30\,000$ K as a function of density is depicted for sDFT and dDFT (using VASP) in the left panel of Fig. 5. The two curves are generally close. The more significant difference in the lower-pressure estimates stems primarily from the smaller cutoff energy used in our calculation. The equation of state can be fitted by a van der Waals form, $P = P_{\text{ideal}}(1 + \frac{\rho}{\rho_0})$ with $\rho_0 = 0.87$ g/cm^3.

The right panel of Fig. 5 illustrates the radial distribution for hydrogen at $T = 30\,000$ K, with varying densities from 0.25 to 16 g/cm^3. At the lowest density, it reveals a relatively large excluded volume with some corrugated pattern. As the density increases to 1 g/cm^3, the radial distribution curve steepens as the proton-proton repulsion range shortens, and the corrugated pattern largely dies out, leaving a shallow signature of a correlation shell at r = 1.5 Å. This feature is enhanced and contracts to a shorter distance of 0.75 Å at the density of 4 g/cm^3. In this regime, the radial distribution signifies a combined short-range repulsion and longer-range attraction between pairs, typical of a gas. Finally, at the highest density considered, 16 g/cm^3, the correlation shell contracts further to 0.5 Å while a second correlation shell seems to form 0.9 Å, hence a radial distribution typical of a liquid emerges at these high densities.

We now turn to studying hydrogen conductivity using Drude's theory of metals [105] as a reference point. Drude's theory gives the real part of the normalized conductivity at frequency ω as

$$\frac{\text{Re}\sigma(\omega)}{n} = \frac{e^2}{m_e}\frac{\tau_c}{1+\omega^2\tau_c^2}, \tag{32}$$

where $n = \frac{N_e}{\Omega}$ is the average electron density, and τ_c, the collision time, is the only material parameter. τ_c is assumed to be independent of n. In Fig. 6 (left panel) we plot our stochastic estimates of the *ab initio* normalized conductivity for hydrogen in various densities at 30 000 K. While the normalized conductivity in Drude's theory [Eq. (32)] does not depend on n, the *ab initio* dc normalized conductivity does depend on it: it changes fourfold as n changes 64-fold. Yet, as seen in Fig. 6, at $\hbar\omega = 7.2$ eV, all four *ab initio* curves cross at approximately the same point, the *isosbestic*

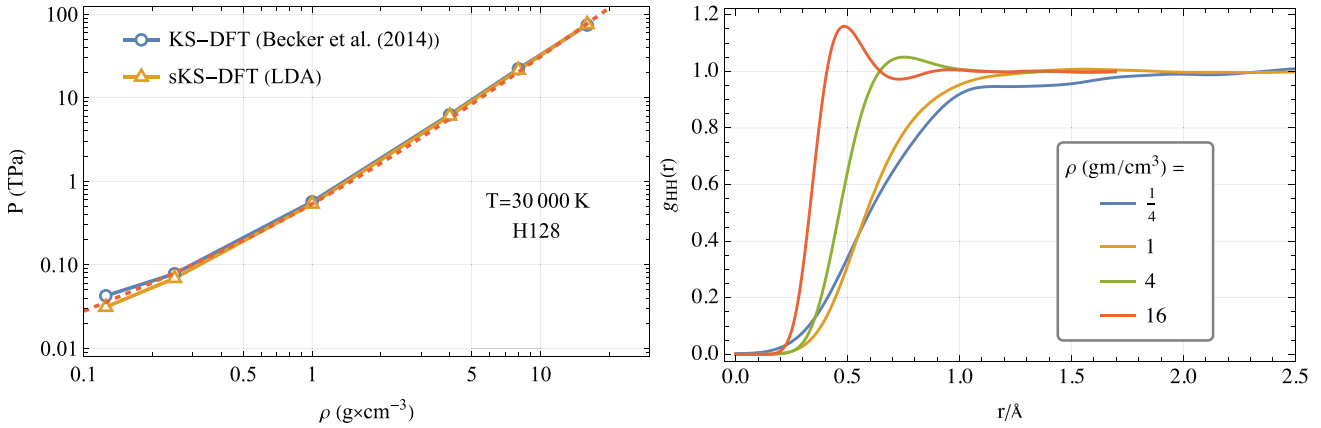

FIG. 5. Left panel: the estimated pressure as a function of density for hydrogen at $T = 30,000$ K. The results of the sDFT calculations are shown together with the calculations taken from Ref. [13] and a dotted van der Waals trend of $P(\rho) = \frac{\rho}{m_p} k_B T (1 + \frac{\rho}{\rho_0})$, where $\rho_0 = 0.87$ g/cm^3 is obtained by fitting. Right panel: the H-H radial distribution for different densities.

point, where they assume *the same* normalized conductivity value of 0.6×10^{-3} Sa$_0^2$. The existence of the isosbestic point, especially in the rather large density range seen here, is sometimes indicative of a system composed of two phases or two states [106–108]. The value of τ_c at the isosbestic point is equal to $(0.084 \pm 0.035i)$ fs, with the real part small relative to typical values of τ_c for room-temperature metals (between 1 and 10 fs [105]). This result is consistent with the dense metal (with r_s between 0.28 and 0.7) we have, and the high temperatures should speed up relaxation times and shorten mean free paths in the material. Equation (32) also shows that Reσ is proportional to ω^{-2} for high frequencies, $\omega\tau_c \gg 1$ (in our case, $\hbar\omega > 30$ eV). As seen in the inset of the figure, the *ab initio* conductivity decreases faster than the Drude second power law in the frequency.

The relative statistical errors in the conductivity evaluation (before stabilization according to the method of Appendix C) are shown in the right panel of the figure. In general, they grow with the density of the gas. Remarkably, the dc conductivity, calculated through Eq. (31), has a much smaller statistical error than the ac conductivity.

VI. SUMMARY

We developed a linear-scaling stochastic DFT implementation in periodic boundary conditions combined with Langevin dynamics, which we applied to hydrogen at 30 000 K. Our pressure estimates at various hydrogen densities between 0.125 and 16 g/cm^3 matched well with results based on deterministic DFT for a high cutoff energy (near convergence). The sensitivity to the cutoff energy reduced as the density increased.

The pair correlation functions showed that hydrogen exhibits gaslike behavior at densities below 4 g/cm^3 and liquidlike behavior above it. We also developed a stochastic method to estimate the Kubo-Greenwood conductivity with minimal statistical noise at $\omega \to 0$. All the calculations were done in the Baldereschi k-point, and then the overall size effects in the hydrogen systems were not large once H_{512} was used, except for the high density, which required a large number of atoms.

Future work will focus on adapting stochastic time-dependent DFT [109–111] and Green's function

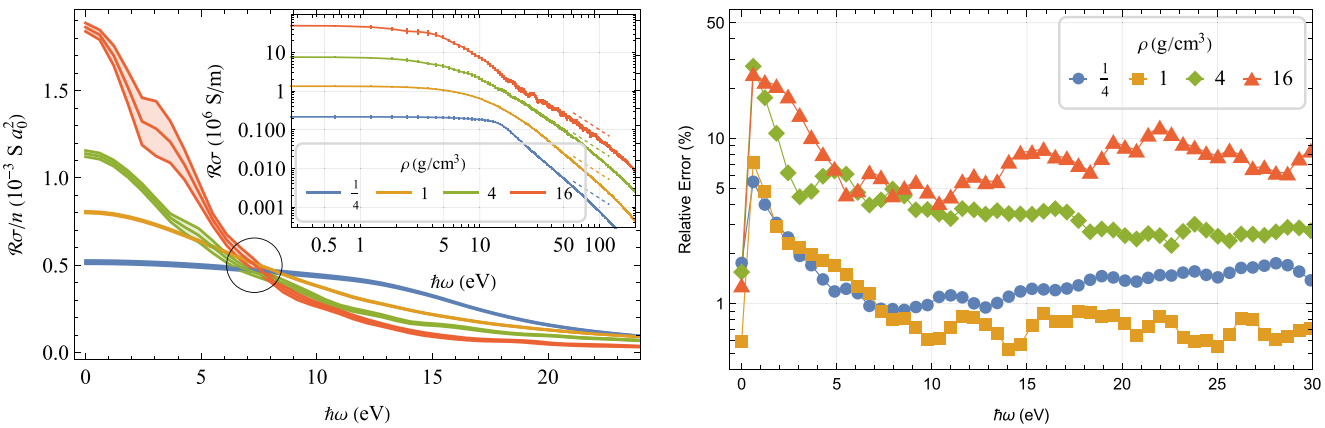

FIG. 6. Left panel: The real part of the Kubo-Greenwood conductivity normalized by the electron density at $T = 30\,000$ K. The black circle indicates an *isosbestic point*, which appears at 7.2 eV, where all systems have the same normalized conductivity of $\sim 0.5 \times 10^{-3}$ Sa$_0^2$. The inset shows the conductivity in log-log scale, with dashed lines indicating slopes of ω^{-2}. Right panel: The relative error bars for the conductivity calculations, as described in the caption of Fig. 4.

methodologies [112–114] for WDM applications, building on the foundation of our current work.

ACKNOWLEDGMENTS

R.B., R.E.H., A.R., and R.R. thank the German Israel Foundation for funding this project. E.R. acknowledges support from the Center for Computational Study of Excited-State Phenomena in Energy Materials (C2SEPEM) at the Lawrence Berkeley National Laboratory, funded by the U.S. Department of Energy, Office of Science, Basic Energy Sciences, Materials Sciences and Engineering Division, under Contract No. DE-AC02-05CH11231, as part of the Computational Materials Sciences Program.

APPENDIX A: PROOF OF EQ. (26)

For noninteracting electrons, the Hamiltonian and the grand-canonical distribution are

$$H=\sum_i \varepsilon_i n_i, \quad n_i \equiv a_i^\dagger a_i, \quad N=\sum_i n_i, \quad \rho=\frac{e^{-\beta(H-N\mu)}}{\mathrm{tr}[e^{-\beta(H-N\mu)}]},$$

where a_i ($a_i^\dagger$) are electron annihilation (creation) operators into eigenstates of the Hamiltonian, with the standard anticommutation relations $\{a_i, a_j\} = \{a_i^\dagger, a_j^\dagger\} = 0$, $\{a_i a_j^\dagger\} = \delta_{ij}$.

From these relations alone, we find the following:

$$[a_i^\dagger a_j, a_k^\dagger a_l] = \delta_{jk} a_i^\dagger a_l - \delta_{il} a_k^\dagger a_j, \tag{A1}$$

$$\mathrm{tr}[\rho a_i^\dagger a_l] = \delta_{il}\mathrm{tr}[\rho n_i] \equiv \delta_{il} p_{\mu\beta}(\varepsilon_i), \tag{A2}$$

and

$$e^{iHt} a_k^\dagger a_l e^{-iHt} = e^{-i(\varepsilon_l-\varepsilon_k)t} a_k^\dagger a_l. \tag{A3}$$

From Eqs. (A1) and (A2),

$$\mathrm{tr}[\rho[a_i^\dagger a_j, a_k^\dagger a_l]] = \left(p^i_{\mu\beta} - p^j_{\mu\beta}\right)\delta_{jk}\delta_{il} \tag{A4}$$

and

$$\mathrm{tr}[\rho[a_i^\dagger a_j, a_k^\dagger(t) a_l(t)]] = e^{i(\varepsilon_i-\varepsilon_j)t/\hbar}\left(p^i_{\mu\beta} - p^j_{\mu\beta}\right)\delta_{jk}\delta_{il}. \tag{A5}$$

Therefore, first quantization (single-particle) observables $\mathcal{A}$ and $\mathcal{B}$, summed over all electrons $\mathcal{A} = \sum_n \mathcal{A}_n$ and $\mathcal{B} = \sum_n \mathcal{B}_n$, correspond in second quantization to $\hat{A} = a_i^\dagger a_j A^{ij}$ and $\hat{B} = a_i^\dagger a_j B^{ij}$ ($A^{ij} = \langle i|\mathcal{A}|j\rangle$ and $B^{ij} = \langle i|\mathcal{B}|j\rangle$). We find from Eq. (A4)

$$\mathrm{tr}[\rho[\hat{A}, \hat{B}]] = \mathrm{Tr}[p_{\mu\beta}(\mathcal{H})[\mathcal{A}, \mathcal{B}]],$$

and from these,

$$\mathrm{Im}\,\mathrm{tr}[\rho\hat{A}\hat{B}] = \mathrm{Im}\,\mathrm{Tr}[p_{\mu\beta}(\mathcal{H})\mathcal{A}\mathcal{B}]. \tag{A6}$$

Using Eq. (A3) we obtain the generalization of Eq. (A6),

$$\mathrm{Im}\,\mathrm{tr}[\rho\hat{A}\hat{B}(t)] = \mathrm{Im}\,\mathrm{Tr}[p_{\mu\beta}(\mathcal{H})\mathcal{A}\mathcal{B}(t)]. \tag{A7}$$

This latter equation, used with $\hat{A} \to \sum_n \mathcal{R}_{n\xi}$ and $\hat{B} \to \sum_n \mathcal{V}_{n\xi'}$, gives Eq. (26).

APPENDIX B: PROOF OF EQ. (31)

The Fourier-transform of Eq. (A5) gives

$$\int_{-\infty}^{\infty} e^{-i\omega t}\mathrm{tr}[\rho[a_i^\dagger a_j, e^{iHt} a_k^\dagger a_l e^{-iHt}]]dt = 2\pi\delta\left(\frac{\varepsilon_i-\varepsilon_j}{\hbar}+\omega\right)[p_{\mu\beta}(\varepsilon_j-\hbar\omega) - p_{\mu\beta}(\varepsilon_j)]\delta_{jk}\delta_{il},$$

where we used the spectral representation of Dirac delta functions, $2\pi\delta(\omega) = \int_{-\infty}^{\infty} e^{-i\omega t}dt$, and the identity $\delta(x-y)f(x) = \delta(x-y)f(y)$. Dividing the above expression by $i\omega$ and taking the limit $\omega \to 0$, we find

$$\lim_{\omega\to 0}\frac{1}{i\omega}\int_{-\infty}^{\infty} e^{-i\omega t}\mathrm{tr}[\rho[a_i^\dagger a_j, e^{iHt} a_k^\dagger a_l e^{-iHt}]]dt = 2\pi\hbar i\delta\left(\frac{\varepsilon_i-\varepsilon_j}{\hbar}\right)p'_{\mu\beta}(\varepsilon_j)\delta_{jk}\delta_{il}.$$

Using the spectral representation in the reverse direction, we find

$$\lim_{\omega\to 0}\frac{1}{i\omega}\int_{-\infty}^{\infty} e^{-i\omega t}\mathrm{tr}[\rho[a_i^\dagger a_j, e^{iHt} a_k^\dagger a_l e^{-iHt}]]dt = i\hbar\int_{-\infty}^{\infty} e^{-i(\varepsilon_i-\varepsilon_j)t}p'_{\mu\beta}(\varepsilon_j)dt\,\delta_{jk}\delta_{il}.$$

From these, it is now straightforward to show the two one-body observables

$$\lim_{\omega\to 0}\frac{1}{i\omega}\int_{-\infty}^{\infty} e^{-i\omega t}\mathrm{tr}[\rho[\hat{A}, \hat{B}(t)]]dt = i\hbar\int_{-\infty}^{\infty}\mathrm{Tr}[p'_{\mu\beta}(\mathcal{H})\mathcal{B}(t)\mathcal{A}]dt. \tag{B1}$$

For the case $A = B$, the left-hand side can be developed to give an integral over positive times,

$$\lim_{\omega\to 0}\frac{1}{i\omega}\int_{-\infty}^{\infty} e^{-i\omega t}\mathrm{tr}[\rho[\hat{A}, \hat{A}(t)]]dt = 4i\,\mathrm{Re}\left[\lim_{\omega\to 0}\frac{1}{i\omega}\int_0^{\infty} e^{-i\omega t}\mathrm{Im}\,\mathrm{tr}[\rho\hat{A}\hat{A}(t)]dt\right]. \tag{B2}$$

The right-hand side of Eq. (B1) can also be developed in a similar fashion:

$$i\hbar\int_{-\infty}^{\infty}\mathrm{Tr}[p'_{\mu\beta}(\mathcal{H})\mathcal{A}(t)\mathcal{A}]dt = 2i\hbar\,\mathrm{Re}\int_0^{\infty}\mathrm{Tr}[p'_{\mu\beta}(\mathcal{H})\mathcal{A}\mathcal{A}(t)]dt. \tag{B3}$$

Equating both right sides,

$$\mathrm{Re}\left[\lim_{\omega\to 0}\frac{1}{i\omega}\int_0^\infty e^{-i\omega t}\,\mathrm{Im\,tr}[\rho\hat{A}\hat{A}(t)]dt\right]=\frac{\hbar}{2}\mathrm{Re}\int_0^\infty \mathrm{Tr}[p'_{\mu\beta}(\mathcal{H})\mathcal{A}\mathcal{A}(t)]dt.$$

Finally, using Eq. (A7), we obtain

$$\mathrm{Re}\left[\lim_{\omega\to 0}\frac{1}{i\omega}\int_0^\infty e^{-i\omega t}dt\,\mathrm{Im\,tr}[p_{\mu\beta}(\mathcal{H})\mathcal{A}\mathcal{A}(t)]\right]=\frac{\hbar}{2}\int_0^\infty \mathrm{Re\,Tr}[p'_{\mu\beta}(\mathcal{H})\mathcal{A}\mathcal{A}(t)]dt, \tag{B4}$$

from which Eq. (31) can be directly deduced.

APPENDIX C: STABILIZING THE LOW-FREQUENCY CONDUCTIVITY SPECTRUM

One of the practical problems in calculating the conductivity at low frequencies arises in connection with introducing a finite resolution parameter ν in Eq. (29). The finite resolution distorts and usually underestimates the conductivity. This is seen in the red empty dots of Fig. 4, which shows reduced conductivity as $\omega\to 0$.

A second problem involves the fact that our conductivity calculations use a stochastic approach, which has fluctuation errors. For low frequency, these fluctuations grow considerably as $\omega\to 0$ (see the right panel of Fig. 6) due to the division by ω in Eq. (27).

The two problems described above combine: the high fluctuations in the low-frequency part of the ac conductivity are exacerbated when we take smaller ν, needed for converging the ac results to the dc limit.

Here, we introduce an approximation that helps converge the low-frequency ac conductivity, which relies on the fact that the dc conductivity ($\omega=0$), calculated by a different expression, Eq. (31), has finite and small fluctuations (seen in the right panel of Fig. 6). Our stabilization procedure mixes the low-frequency conductivity with that of an optimized model:

$$\sigma_k\leftarrow(1-w_k)\sigma_k+w_k\sigma_{\mathrm{model}}(\omega_k),$$

where σ_k is the conductivity corresponding to the frequency $\omega_k=k\nu$, $k=0,1,2,\ldots$. Here, w_k are mixing weights

$$w_k=\frac{1}{1+\left(\frac{\omega_k}{\omega_c}\right)^6},$$

emphasizing the low-energy spectrum. Since our system exhibits a metallic behavior, we choose ω_c as the highest frequency in the spectrum for which $\sigma_c>0.7\sigma_0$, and we use the Drude model $\sigma_{\mathrm{model}}(\omega)=\frac{\sigma_0}{1+\omega^2\tau_c^2}$, depending on the single parameter τ_c, i.e., the collision time. Given the calculated spectrum, we set this parameter as follows:

$$\tau_c^2=\frac{\sum_k w_k\omega_k^2\sigma_k(\sigma_0-\sigma_k)}{\sum_k w_k\omega_k^4\sigma_k^2}.$$

With this choice of parameter, the calculated conductivity values σ_k are as close as possible, in the root-mean-square sense, to those of the model conductivity $\sigma_{\mathrm{model}}(\omega_k)$ because we minimize the Lagrangian $L(\tau_c^2)=\sum_k w_k[(1+\omega_k^2\tau_c^2)\sigma_k-\sigma_0]^2$.

[1] T. Guillot, Interiors of giant planets inside and outside the solar system, Science **286**, 72 (1999).

[2] J. H. Nguyen and N. C. Holmes, Melting of iron at the physical conditions of the Earth's core, Nature (London) **427**, 339 (2004).

[3] R. Redmer, T. R. Mattsson, N. Nettelmann, and M. French, The phase diagram of water and the magnetic fields of Uranus and Neptune, Icarus **211**, 798 (2011).

[4] M. Pozzo, C. Davies, D. Gubbins, and D. Alfè, Thermal and electrical conductivity of iron at Earth's core conditions, Nature (London) **485**, 355 (2012).

[5] A. Benuzzi-Mounaix, S. Mazevet, A. Ravasio, T. Vinci, A. Denoeud, M. Koenig, N. Amadou, E. Brambrink, F. Festa, A. Levy, M. Harmand, S. Brygoo, G. Huser, V. Recoules, J. Bouchet, G. Morard, F. Guyot, T. De Resseguier, K. Myanishi, N. Ozaki, F. Dorchies, J. Gaudin, P. M. Leguay, O. Peyrusse, O. Henry, D. Raffestin, S. L. Pape, R. Smith, and R. Musella, Progress in warm dense matter study with applications to planetology, Phys. Scr. **T161**, 014060 (2014).

[6] M. French and N. Nettelmann, Viscosity and prandtl number of warm dense water as in ice giant planets, Astrophys. J. **881**, 81 (2019).

[7] D. Ehrenreich, C. Lovis, R. Allart, M. R. Z. Osorio, F. Pepe, S. Cristiani, R. Rebolo, N. C. Santos, F. Borsa, O. Demangeon, X. Dumusque, J. I. G. Hernández, N. Casasayas-Barris, D. Ségransan, S. Sousa, M. Abreu, V. Adibekyan, M. Affolter, C. A. Prieto, Y. Alibert, M. Aliverti, D. Alves, M. Amate, G. Avila, V. Baldini, T. Bandy, W. Benz, A. Bianco, E. Bolmont *et al.*, Nightside condensation of iron in an ultrahot giant exoplanet, Nature (London) **580**, 597 (2020).

[8] J. J. Fortney and N. Nettelmann, The interior structure, composition, and evolution of giant planets, Space Sci. Rev. **152**, 423 (2010).

[9] M. Bethkenhagen, E. R. Meyer, S. Hamel, N. Nettelmann, M. French, L. Scheibe, C. Ticknor, L. A. Collins, J. D. Kress, J. J. Fortney, and R. Redmer, Planetary ices and the linear mixing approximation, Astrophys. J. **848**, 67 (2017).

[10] M. French, A. Becker, W. Lorenzen, N. Nettelmann, M. Bethkenhagen, J. Wicht, and R. Redmer, *Ab initio* simulations for the material properties along jupiter's adiabat, Astrophys. J. Suppl. Series **202**, 5 (2012).

[11] D. Saumon, W. B. Hubbard, G. Chabrier, and H. M. van Horn, The role of the molecular-metallic transition of hydrogen in the evolution of jupiter, saturn, and brown dwarfs, Astrophys. J. **391**, 827 (1992).

[12] S. R. Kulkarni, Brown dwarfs: A possible missing link between stars and planets, Science **276**, 1350 (1997).

[13] A. Becker, W. Lorenzen, J. J. Fortney, N. Nettelmann, M. Schöttler, and R. Redmer, *Ab initio* equations of state for hydrogen (H-REOS.3) and helium (He-REOS.3) and their

implications for the interior of brown dwarfs, Astrophys. J. Suppl. Series **215**, 21 (2014).
[14] N. Booth, A. P. L. Robinson, P. Hakel, R. J. Clarke, R. J. Dance, D. Doria, L. A. Gizzi, G. Gregori, P. Koester, L. Labate, T. Levato, B. Li, M. Makita, R. C. Mancini, J. Pasley, P. P. Rajeev, D. Riley, E. Wagenaars, J. N. Waugh, and N. C. Woolsey, Laboratory measurements of resistivity in warm dense plasmas relevant to the microphysics of brown dwarfs, Nat. Commun. **6**, 8742 (2015).
[15] A. Becker, M. Bethkenhagen, C. Kellermann, J. Wicht, and R. Redmer, Material properties for the interiors of massive giant planets and brown dwarfs, Astrophys. J. **156**, 149 (2018).
[16] G. Chabrier, Quantum effects in dense coulombic matter: Application to the cooling of white dwarfs, Astrophys. J. **414**, 695 (1993).
[17] D. Saumon, S. Blouin, and P.-E. Tremblay, Current challenges in the physics of white dwarf stars, Phys. Rep. **988**, 1 (2022).
[18] D. E. Hinkel, Scientific and technological advancements in inertial fusion energy, Nucl. Fusion **53**, 104027 (2013).
[19] J. Lindl, Development of the indirect-drive approach to inertial confinement fusion and the target physics basis for ignition and gain, Phys. Plasmas **2**, 3933 (1995).
[20] E. M. Campbell, V. N. Goncharov, T. C. Sangster, S. P. Regan, P. B. Radha, R. Betti, J. F. Myatt, D. H. Froula, M. J. Rosenberg, I. V. Igumenshchev, W. Seka, A. A. Solodov, A. V. Maximov, J. A. Marozas, T. J. B. Collins, D. Turnbull, F. J. Marshall, A. Shvydky, J. P. Knauer, R. L. McCrory, A. B. Sefkow, M. Hohenberger, P. A. Michel, T. Chapman, L. Masse, C. Goyon, S. Ross, J. W. Bates, M. Karasik, J. Oh, J. Weaver, A. J. Schmitt, K. Obenschain, S. P. Obenschain, S. Reyes, and B. Van Wonterghem, Laser-direct-drive program: Promise, challenge, and path forward, Matter Radiat. Extremes **2**, 37 (2017).
[21] B. A. Remington, R. M. Cavallo, M. J. Edwards, D. D.-M. Ho, B. F. Lasinski, K. T. Lorenz, H. E. Lorenzana, J. M. McNaney, S. M. Pollaine, and R. F. Smith, Accessing high pressure states relevant to core conditions in the giant planets, Astrophys. Space Sci. **298**, 235 (2005).
[22] K. Falk, Experimental methods for warm dense matter research, High Pow. Laser Sci. Eng. **6**, e59 (2018).
[23] B. Militzer, D. M. Ceperley, J. D. Kress, J. D. Johnson, L. A. Collins, and S. Mazevet, Calculation of a deuterium double shock hugoniot from *ab initio* simulations, Phys. Rev. Lett. **87**, 275502 (2001).
[24] B. Holst, R. Redmer, and M. P. Desjarlais, Thermophysical properties of warm dense hydrogen using quantum molecular dynamics simulations, Phys. Rev. B **77**, 184201 (2008).
[25] M. A. Morales, C. Pierleoni, and D. M. Ceperley, Equation of state of metallic hydrogen from coupled electron-ion Monte Carlo simulations, Phys. Rev. E **81**, 021202 (2010).
[26] E. Brown, M. A. Morales, C. Pierleoni, and D. Ceperley, Quantum Monte Carlo techniques and applications for warm dense matter, in *Frontiers and Challenges in Warm Dense Matter*, edited by F. Graziani, M. P. Desjarlais, R. Redmer, and S. B. Trickey (Springer International, Cham, 2014), pp. 123–149.
[27] M. Bethkenhagen, B. B. L. Witte, M. Schörner, G. Röpke, T. Döppner, D. Kraus, S. H. Glenzer, P. A. Sterne, and R. Redmer, Carbon ionization at gigabar pressures: An *ab initio* perspective on astrophysical high-density plasmas, Phys. Rev. Res. **2**, 023260 (2020).
[28] M. Tuckerman, *Statistical Mechanics: Theory and Molecular Simulation* (Oxford University Press, Oxford, 2010).
[29] H. Niu, Y. Yang, S. Jensen, M. Holzmann, C. Pierleoni, and D. M. Ceperley, Stable solid molecular hydrogen above 900 K from a machine-learned potential trained with diffusion quantum Monte Carlo, Phys. Rev. Lett. **130**, 076102 (2023).
[30] C. J. Pickard and R. J. Needs, Structure of phase III of solid hydrogen, Nat. Phys. **3**, 473 (2007).
[31] K.-P. Bohnen, M. Kiwi, and H. Suhl, Friction coefficient of an adsorbed h atom on a metal surface, Phys. Rev. Lett. **34**, 1512 (1975).
[32] M. P. Grumbach, D. Hohl, R. M. Martin, and R. Car, Ab initio molecular dynamics with a finite-temperature density functional, J. Phys.: Condens. Matter **6**, 1999 (1994).
[33] B. Hellsing and M. Persson, Electronic damping of atomic and molecular vibrations at metal surfaces, Phys. Scr. **29**, 360 (1984).
[34] R. Baer and N. Siam, Real-time study of the adiabatic energy loss in an atomic collision with a metal cluster, J. Chem. Phys. **121**, 6341 (2004).
[35] F. Becca and S. Sorella, *Quantum Monte Carlo Approaches for Correlated Systems*, 1st ed. (Cambridge University Press, 2017).
[36] V. V. Karasiev, T. Sjostrom, D. Chakraborty, J. Dufty, K. Runge, F. E. Harris, and S. B. Trickey, Innovations in finite-temperature density functionals, in *Frontiers and Challenges in Warm Dense Matter*, *Vol. 96 of Lecture Notes in Computational Science and Engineering* (Springer Science & Business, 2014).
[37] P. Geerlings, F. De Proft, and W. Langenaeker, Conceptual density functional theory, Chem. Rev. **103**, 1793 (2003).
[38] R. M. Martin, *Electronic Structure: Basic Theory and Practical Methods* (Cambridge University Press, Cambridge, UK, 2004).
[39] J. Hutter, Car-Parrinello molecular dynamics, WIREs Comput. Mol. Sci. **2**, 604 (2012).
[40] A. Pribram-Jones, D. A. Gross, and K. Burke, DFT: A theory full of holes? Annu. Rev. Phys. Chem. **66**, 283 (2015).
[41] R. M. Martin, L. Reining, and D. M. Ceperley, *Interacting Electrons* (Cambridge University Press, 2016).
[42] F. Jensen, *Introduction to Computational Chemistry*, 3rd ed. (Wiley, Chichester, UK, 2017).
[43] O. A. von Lilienfeld, K.-R. Müller, and A. Tkatchenko, Exploring chemical compound space with quantum-based machine learning, Nat. Rev. Chem. **4**, 347 (2020).
[44] J. P. Perdew and M. Levy, Physical content of the exact kohn-sham orbital energies: Band gaps and derivative discontinuities, Phys. Rev. Lett. **51**, 1884 (1983).
[45] L. Kronik, T. Stein, S. Refaely-Abramson, and R. Baer, Excitation gaps of finite-sized systems from optimally tuned range-separated hybrid functionals, J. Chem. Theor.y Comput. **8**, 1515 (2012).
[46] N. D. Mermin, Thermal properties of the inhomogeneous electron gas, Phys. Rev. **137**, A1441 (1965).
[47] S. Pittalis, C. R. Proetto, A. Floris, A. Sanna, C. Bersier, K. Burke, and E. K. U. Gross, Exact conditions in finite-temperature density-functional theory, Phys. Rev. Lett. **107**, 163001 (2011).

[48] A. Pribram-Jones, S. Pilatis, E. K. U. Gross, and K. Burke, Thermal density functional theory in context, in *Frontiers and Challenges in Warm Dense Matter*, Vol. 96 of *Lecture Notes in Computational Science and Engineering* (Springer Science & Business, Cham, 2014).

[49] S. Groth, T. Dornheim, T. Sjostrom, F. D. Malone, W. M. C. Foulkes, and M. Bonitz, Ab initio exchange-correlation free energy of the uniform electron gas at warm dense matter conditions, Phys. Rev. Lett. **119**, 135001 (2017).

[50] M. Bonitz, T. Dornheim, Z. A. Moldabekov, S. Zhang, P. Hamann, H. Kählert, A. Filinov, K. Ramakrishna, and J. Vorberger, *Ab initio* simulation of warm dense matter, Phys. Plasmas **27**, 042710 (2020).

[51] Z. Moldabekov, T. Dornheim, J. Vorberger, and A. Cangi, Benchmarking exchange-correlation functionals in the spin-polarized inhomogeneous electron gas under warm dense conditions, Phys. Rev. B **105**, 035134 (2022).

[52] S. Zhang, H. Wang, W. Kang, P. Zhang, and X. T. He, Extended application of Kohn-Sham first-principles molecular dynamics method with plane wave approximation at high energy—From cold materials to hot dense plasmas, Phys. Plasmas **23**, 042707 (2016).

[53] A. Blanchet, J. Clérouin, M. Torrent, and F. Soubiran, Extended first-principles molecular dynamics model for high temperature simulations in the Abinit code: Application to warm dense aluminum, Comput. Phys. Commun. **271**, 108215 (2022).

[54] R. P. Feynman, N. Metropolis, and E. Teller, Equations of state of elements based on the generalized Fermi-Thomas theory, Phys. Rev. **75**, 1561 (1949).

[55] F. Perrot, Gradient correction to the statistical electronic free energy at nonzero temperatures: Application to equation-of-state calculations, Phys. Rev. A **20**, 586 (1979).

[56] V. V. Karasiev, T. Sjostrom, and S. B. Trickey, Generalized-gradient-approximation noninteracting free-energy functionals for orbital-free density functional calculations, Phys. Rev. B **86**, 115101 (2012).

[57] T. Sjostrom and J. Daligault, Fast and accurate quantum molecular dynamics of dense plasmas across temperature regimes, Phys. Rev. Lett. **113**, 155006 (2014).

[58] V. V. Karasiev, D. Chakraborty, O. A. Shukruto, and S. B. Trickey, Nonempirical generalized gradient approximation free-energy functional for orbital-free simulations, Phys. Rev. B **88**, 161108(R) (2013).

[59] K. Luo, V. V. Karasiev, and S. B. Trickey, Towards accurate orbital-free simulations: A generalized gradient approximation for the noninteracting free energy density functional, Phys. Rev. B **101**, 075116 (2020).

[60] V. L. Ligneres and E. A. Carter, An introduction to orbital-free density functional theory, in *Handbook of Materials Modeling*, edited by S. Yip (Springer, Dordrecht, Berlin, 2005), pp. 137–148.

[61] F. Lambert, J. Clérouin, and G. Zérah, Very-high-temperature molecular dynamics, Phys. Rev. E **73**, 016403 (2006).

[62] C. Ticknor, J. D. Kress, L. A. Collins, J. Clérouin, P. Arnault, and A. Decoster, Transport properties of an asymmetric mixture in the dense plasma regime, Phys. Rev. E **93**, 063208 (2016).

[63] S. X. Hu, R. Gao, Y. Ding, L. A. Collins, and J. D. Kress, First-principles equation-of-state table of silicon and its effects on high-energy-density plasma simulations, Phys. Rev. E **95**, 043210 (2017).

[64] A. J. White, O. Certik, Y. H. Ding, S. X. Hu, and L. A. Collins, Time-dependent orbital-free density functional theory for electronic stopping power: Comparison to the Mermin-Kohn-Sham theory at high temperatures, Phys. Rev. B **98**, 144302 (2018).

[65] A. J. White, C. Ticknor, E. R. Meyer, J. D. Kress, and L. A. Collins, Multicomponent mutual diffusion in the warm, dense matter regime, Phys. Rev. E **100**, 033213 (2019).

[66] W. Mi, K. Luo, S. B. Trickey, and M. Pavanello, Orbital-free density functional theory: An attractive electronic structure method for large-scale first-principles simulations, Chem. Rev. **123**, 12039 (2023).

[67] B. Cheng, G. Mazzola, C. J. Pickard, and M. Ceriotti, Evidence for supercritical behaviour of high-pressure liquid hydrogen, Nature (London) **585**, 217 (2020).

[68] O. A. von Lilienfeld and K. Burke, Retrospective on a decade of machine learning for chemical discovery, Nat. Commun. **11**, 4895 (2020).

[69] V. V. Karasiev, J. Hinz, S. X. Hu, and S. B. Trickey, On the liquid–liquid phase transition of dense hydrogen, Nature (London) **600**, E12 (2021).

[70] J. A. Ellis, L. Fiedler, G. A. Popoola, N. A. Modine, J. A. Stephens, A. P. Thompson, A. Cangi, and S. Rajamanickam, Accelerating finite-temperature Kohn-Sham density functional theory with deep neural networks, Phys. Rev. B **104**, 035120 (2021).

[71] B. Cheng, S. Hamel, and M. Bethkenhagen, Thermodynamics of diamond formation from hydrocarbon mixtures in planets, Nat. Commun. **14**, 1104 (2023).

[72] R. Baer, D. Neuhauser, and E. Rabani, Self-averaging stochastic kohn-sham density-functional theory, Phys. Rev. Lett. **111**, 106402 (2013).

[73] Y. Cytter, E. Rabani, D. Neuhauser, and R. Baer, Stochastic density functional theory at finite temperatures, Phys. Rev. B **97**, 115207 (2018).

[74] Y. Cytter, E. Rabani, D. Neuhauser, M. Preising, R. Redmer, and R. Baer, Transition to metallization in warm dense helium-hydrogen mixtures using stochastic density functional theory within the Kubo-Greenwood formalism, Phys. Rev. B **100**, 195101 (2019).

[75] A. J. White and L. A. Collins, Fast and universal kohn-sham density functional theory algorithm for warm dense matter to hot dense plasma, Phys. Rev. Lett. **125**, 055002 (2020).

[76] M. Chen, R. Baer, D. Neuhauser, and E. Rabani, Stochastic density functional theory: Real- and energy-space fragmentation for noise reduction, J. Chem. Phys. **154**, 204108 (2021).

[77] R. Baer, D. Neuhauser, and E. Rabani, Stochastic vector techniques in ground-state electronic structure, Annu. Rev. Phys. Chem. **73**, 255 (2022).

[78] T. Chen, Q. Liu, Y. Liu, L. Sun, and M. Chen, Combining stochastic density functional theory with deep potential molecular dynamics to study warm dense matter, Matter Radiat. Extremes **9**, 015604 (2024).

[79] P. Hohenberg and W. Kohn, Inhomogeneous electron gas, Phys. Rev. **136**, B864 (1964).

[80] W. Kohn and L. J. Sham, Self-consistent equations including exchange and correlation effects, Phys. Rev. **140**, A1133 (1965).

[81] N. Argaman and G. Makov, Thermodynamics as an alternative foundation for zero-temperature density-functional theory and spin-density-functional theory, Phys. Rev. B **66**, 052413 (2002).
[82] M. Weinert and J. W. Davenport, Fractional occupations and density-functional energies and forces, Phys. Rev. B **45**, 13709 (1992).
[83] V. V. Karasiev, T. Sjostrom, J. Dufty, and S. B. Trickey, Accurate homogeneous electron gas exchange-correlation free energy for local spin-density calculations, Phys. Rev. Lett. **112**, 076403 (2014).
[84] V. V. Karasiev, L. Calderín, and S. B. Trickey, Importance of finite-temperature exchange correlation for warm dense matter calculations, Phys. Rev. E **93**, 063207 (2016).
[85] V. V. Karasiev, J. W. Dufty, and S. B. Trickey, Nonempirical semilocal free-energy density functional for matter under extreme conditions, Phys. Rev. Lett. **120**, 076401 (2018).
[86] K. Ramakrishna, T. Dornheim, and J. Vorberger, Influence of finite temperature exchange-correlation effects in hydrogen, Phys. Rev. B **101**, 195129 (2020).
[87] J. Hinz, V. V. Karasiev, S. X. Hu, M. Zaghoo, D. Mejía-Rodríguez, S. B. Trickey, and L. Calderín, Fully consistent density functional theory determination of the insulator-metal transition boundary in warm dense hydrogen, Phys. Rev. Res. **2**, 032065(R) (2020).
[88] V. V. Karasiev, D. I. Mihaylov, and S. X. Hu, Meta-GGA exchange-correlation free energy density functional to increase the accuracy of warm dense matter simulations, Phys. Rev. B **105**, L081109 (2022).
[89] D. I. Mihaylov, V. V. Karasiev, and S. X. Hu, Thermal hybrid exchange-correlation density functional for improving the description of warm dense matter, Phys. Rev. B **101**, 245141 (2020).
[90] R. Kosloff, Time-dependent quantum-mechanical methods for molecular-dynamics, J. Phys. Chem. **92**, 2087 (1988).
[91] T. J. Rivlin, *Chebyshev Polynomials: From Approximation Theory to Algebra and Numbers Theory* (Wiley, New York, 1990).
[92] M. Chen, R. Baer, D. Neuhauser, and E. Rabani, Energy window stochastic density functional theory, J. Chem. Phys. **151**, 114116 (2019).
[93] Y. Luo, A. Zen, and S. Sorella, Ab initio molecular dynamics with noisy forces: Validating the quantum Monte Carlo approach with benchmark calculations of molecular vibrational properties, J. Chem. Phys. **141**, 194112 (2014).
[94] R. Kubo, Statistical-mechanical theory of irreversible processes. I. General theory and simple applications to magnetic and conduction problems, J. Phys. Soc. Jpn. **12**, 570 (1957).
[95] D. A. Greenwood, The Boltzmann equation in the theory of electrical conduction in metals, Proc. Phys. Soc. **71**, 585 (1958).
[96] B. Holst, M. French, and R. Redmer, Electronic transport coefficients from *ab initio* simulations and application to dense liquid hydrogen, Phys. Rev. B **83**, 235120 (2011).
[97] L. Calderín, V. V. Karasiev, and S. B. Trickey, Kubo-Greenwood electrical conductivity formulation and implementation for projector augmented wave datasets, Comput. Phys. Commun. **221**, 118 (2017).
[98] G. Kresse and J. Hafner, *Ab initio* molecular dynamics for liquid metals, Phys. Rev. B **47**, 558 (1993).
[99] G. Kresse and J. Hafner, *Ab initio* molecular-dynamics simulation of the liquid-metal–amorphous-semiconductor transition in germanium, Phys. Rev. B **49**, 14251 (1994).
[100] G. Kresse and J. Furthmüller, Efficient iterative schemes for *ab initio* total-energy calculations using a plane-wave basis set, Phys. Rev. B **54**, 11169 (1996).
[101] G. Kresse and J. Furthmüller, Efficiency of ab-initio total energy calculations for metals and semiconductors using a plane-wave basis set, Comput. Mater. Sci. **6**, 15 (1996).
[102] G. Kresse and D. Joubert, From ultrasoft pseudopotentials to the projector augmented-wave method, Phys. Rev. B **59**, 1758 (1999).
[103] N. Troullier and J. L. Martins, Efficient pseudopotentials for plane-wave calculations, Phys. Rev. B **43**, 1993 (1991).
[104] A. Baldereschi, Mean-value point in the brillouin zone, Phys. Rev. B **7**, 5212 (1973).
[105] N. W. Ashcroft and N. David Mermin, *Solid State Physics* (Harcort, Orlando, 1976).
[106] G. W. Robinson, C. H. Cho, and J. Urquidi, Isosbestic points in liquid water: Further strong evidence for the two-state mixture model, J. Chem. Phys. **111**, 698 (1999).
[107] M. Eckstein, M. Kollar, and D. Vollhardt, Isosbestic points in the spectral function of correlated electrons, J. Low Temp. Phys. **147**, 279 (2007).
[108] P. Renati, Z. Kovacs, A. De Ninno, and R. Tsenkova, Temperature dependence analysis of the NIR spectra of liquid water confirms the existence of two phases, one of which is in a coherent state, J. Mol. Liq. **292**, 111449 (2019).
[109] Y. Gao, D. Neuhauser, R. Baer, and E. Rabani, Sublinear scaling for time-dependent stochastic density functional theory, J. Chem. Phys. **142**, 034106 (2015).
[110] V. Vlček, R. Baer, and D. Neuhauser, Stochastic time-dependent DFT with optimally tuned range-separated hybrids: Application to excitonic effects in large phosphorene sheets, J. Chem. Phys. **150**, 184118 (2019).
[111] X. Zhang, G. Lu, R. Baer, E. Rabani, and D. Neuhauser, Linear-response time-dependent density functional theory with stochastic range-separated hybrids, J. Chem. Theor. Comput. **16**, 1064 (2020).
[112] D. Neuhauser, Y. Gao, C. Arntsen, C. Karshenas, E. Rabani, and R. Baer, Breaking the theoretical scaling limit for predicting quasiparticle energies: The stochastic *GW* approach, Phys. Rev. Lett. **113**, 076402 (2014).
[113] E. Rabani, R. Baer, and D. Neuhauser, Time-dependent stochastic Bethe-Salpeter approach, Phys. Rev. B **91**, 235302 (2015).
[114] D. Neuhauser, R. Baer, and D. Zgid, Stochastic self-consistent second-order Green's function method for correlation energies of large electronic systems, J. Chem. Theor. Comput. **13**, 5396 (2017).